HOLOGRAPHIC INTERFEROMETRY FOR COMPUTATIONAL FLUID DYNAMICS MODEL VALIDATION

by

Pal Toth

A thesis submitted to the faculty of
The University of Utah
in partial fulfillment of the requirements for the degree of

Master of Science

Department of Chemical Engineering

The University of Utah

May 2012

The University of Utah Graduate School

STATEMENT OF THESIS APPROVAL

The thesis of **Pal Toth**

has been approved by the following supervisory committee members:

Eric G. Eddings	, Chair	**3/19/2012** Date Approved
Terry A. Ring	, Member	Date Approved
Mikhail Skliar	, Member	**3/19/2012** Date Approved

and by **JoAnn S. Lighty** , Chair of the Department of **Chemical Engineering**

and by Charles A. Wight, Dean of The Graduate School.

ABSTRACT

Consistency analysis and data collaboration is a relatively new scientific area. It deals with quantifying how well scientific models approximate empirical reality. Consistency analysis is based on methodically comparing model predictions with experimental measurements, but this task is made more difficult by the fact that both models and experiments have their own inherent uncertainties. Computational fluid dynamics (CFD) models are numerical methods able to solve complicated discrete fluid dynamics problems. They are used thoroughly in mechanical, aerospace and energy science. As CFD models are being applied to more and more critical systems, there is a growing need to improve the reliability of CFD model predictions. This work addresses this need by presenting consistency analysis results for a simple CFD model and an experiment in which the concentration field of a buoyant helium plume had been studied by holographic interferometry. A detailed procedure is presented for carrying out data collaboration between simulation and experimental data. This work is novel in a sense that it is the first to present the specific difficulties of collaborating interferometric data. These difficulties arise from the encoded nature of information being present in interferometric fringe images.

CONTENTS

CHAPTER 1

INTRODUCTION

Utilizing holographic interferometry for CFD model validation and uncertainty quantification purposes is a complex process, which requires the understanding of the fluid mechanics, optics, photonics, image processing and data collaboration sides of the problem. In this section a systematic overview of all these topics is given, presenting past and historic publications and current challenges in each field.

1.1 Buoyant Plumes

The fluid dynamics of buoyant plumes and jets have been a widely studied area since the early seventies (1). Phenomena in real world applications, such as fuel leakages, fuel injection, pool fires, tank emissions and natural and artificial gas plumes give these studies practical relevance. Because of the typical characteristics of these applications, the phenomenon of injecting lower density fluids into higher density media bears the highest significance. The dominating driving force of the flow in all cases is the buoyant force acting on the lower density fluid.

Early studies characterized the far-field behavior of buoyant plumes. In the far-field concentration and velocity fields achieve self-similarity (2; 3; 4; 5), however, the far-field

behavior depends strongly on near-field processes, which include buoyant effects, diffusion, fluid entrainment, buoyant instabilities and finally transition to turbulent flow.

The near-field region is far less understood than the far-field. There are not as many publications discussing the instabilities of buoyant plumes in or close to the laminar flow region and these publications mostly concentrate on the periodic effects in the flow. Hamins et al. reported that periodic oscillations are not initiated in the plume unless the exit velocity exceeds an experimentally determined limit value (6). Subbarao and Cantwell reported that periodic oscillations only occur in the near-field under specific flow conditions characterized by the Reynolds number (300-1500) and the Richardson number (0.5-6) (7). Cetegen et al. found that the frequency of the periodic oscillations characterized by the Strouhal number was correlated with the Richardson number (8; 9).

The cause of puffing in buoyant plumes is still a subject of debate. Most researchers suggest that the main cause is possibly the Rayleigh-Taylor instability, which is a gravity-driven instability appearing at the interface between two fluids with different densities. Others suggest that the puffing is the combined result of the Rayleigh-Taylor and Kelvin-Helmholtz instabilities, the latter being a shear-driven instability (10).

1.2 Holographic Interferometry

The term interferometry refers to any diagnostic technique that utilizes superimposed, interfering electromagnetic waves to extract information about the analyzed phenomenon of specimen. Interferometric techniques are widely used in astronomy, material testing, seismology, oceanography, quantum mechanics, particle physics and biology.

1.2.1 Fringe Pattern Formation

In interferometry, typically a single coherent electromagnetic beam is split into two beams. The two beams are later united on an appropriate detector plate. One of the beams is called reference beam and the other is called measurement beam. The two beams travel different paths before being united on the detector. The reference beam usually traverses through homogeneous media (e.g., air) without any disrupt changes in its optical properties, while the measurement beam is passed through or reflected from an object of interest. Since we assume that apart from the object of interest there is no significant change in the optical properties of the transmitting media, the phase change of the measurement beam relative to the reference beam will be most strongly determined by the properties of the object in question. After reuniting the beams, an interference pattern or image forms on the detector, from which implications on the properties of the object can be derived. The interference pattern is formed because depending on the phase difference between the two beams, constructive or destructive interference occurs, yielding more intense or less intense signals, respectively (11).

If the above mentioned split beam is a light beam, we call the method optical interferometry. In optical interferometry, a coherent light beam is split into reference and measurement beams and later reunited on an optical detector plate. Since the utilized light must be coherent, intense and convergent, lasers are usually used as emitters. The detector can be simple photoactive sheets or digital detector arrays. Optical interferometry has the advantage that the formed interference array is usually visible by the human eye as the pattern of bright (constructive interference) and dark (destructive interference) lines. Because of the appearance of optical interference patterns, they are

commonly called fringe patterns, where a ‘fringe’ means a continuous dark line (as a result of cancelling beams) on the image.

The term ‘holographic’ refers to the Greek words ‘holo’ (whole) and ‘gramma’ (message), simply meaning that holographic images contain added information compared to simple intensity images. In most cases, the added information comes from the mentioned phase difference (12).

Complete cancellation or destructive interference occurs at a point on the detector if the inclining reference and measurement beams have a phase difference of $n\pi$ and constructive interference occurs at a point if the two beams are at an $N\pi$ phase difference, where n is an odd integer and N is an even integer. Figure 1 illustrates the interference of two superimposed sinusoidal waves. Figure 2 shows some typical fringe patterns (13).

There are two basic types of interferometry: heterodyne and homodyne techniques. In heterodyne methods, one beam among the two is (usually) frequency modulated by shifting its frequency by a small amount. The intensity of the resulting superimposed wave will slowly oscillate at the beat frequency determined by the known modulation. Since the modulation is known, the phase difference between the two original beams can be computed. In homodyne methods, the two beams are at the same frequency (11).

1.2.2 Mathematical Representation of a Fringe Pattern

In the most general case, two-dimensional interferometric fringe patterns can be described by the following equation:

$$i(x,y) = a(x,y) + b(x,y)cos[\psi(x,y) + u_0 x + v_0 y] + N(x,y). \quad [1]$$

This equation describes a two-dimensional intensity (scalar) field *I(x,y)*. The term *a(x,y)* refers to a usually low frequency spatial function, which represents the background illumination. The function *b(x,y)* is also usually a low frequency contributor, representing the slow contrast change of the fringes. The cosine term represents the periodic nature of the fringes themselves and the pattern is modulated by the two-dimensional phase $\psi(x,y)$ and the two carrier frequencies u_0 (in the *x* direction) and v_0 (in the *y* direction). Carrier frequencies are usually present in surface measurement applications, where a pre-generated linear pattern is projected onto the analyzed surface (13). *N(x,y)* appears in real (experimentally obtained) fringe patterns and it represents noise, a high frequency component.

From the above equation it is easy to see that once the phase difference function is known, the fringe pattern can be easily reproduced by taking its cosine. In real applications, the underlying phase information is rarely known (mostly it is the property of interest). From the point of these practical applications, it is important to understand the concept of the 'wrapped' phase. The term simply means that it is the modulo 2π representation of the continuous phase map and its relevance is in the fact that in the inverse problem (where one wants to compute the phase from the fringe pattern) the wrapped phase map is much easier to obtain than the continuous phase map. Figure 3 shows simulated an ideal fringe pattern (without the background illumination, contrast change, noise term and carriers) and underlying phase information. The phase map has

been prepared by Matlab's *peak* function. The fringe pattern is simply its cosine and the wrapped phase is simply its modulo of 2π.

1.3 Obtaining the Unwrapped Phase

In this section an overview of existing phase extracting techniques developed for solving the above outlined inverse problem is given. The available methods vary widely in the applied principles from partial differential equations (14) through local extrema methods (15) to block processing (16) and multigrid techniques (17). In most situations, physical information can be directly extracted from the unwrapped phase map, but it is rarely obtainable directly from the fringe pattern image. The extraction of the wrapped phase is usually carried out as an intermediate step. This intermediate step is usually referred to as the 'demodulation' step.

1.3.1 Basic Digital Image Processing of Fringe Pattern Images

As described in Chapter 2, real fringe patterns are usually corrupted by both low- and high frequency additive and low frequency multiplicative noise. Along with these effects, mostly due to calibration issues or vibration, a process called 'registration' is required before phase analysis. The registration step makes sure that successive images use the same absolute coordinate system. The lack of the registration step can lead to false spatial errors or fluctuations caused by the changing location of the reference axes in the images.

For almost all phase extraction methods the high-frequency additive noise component makes the accuracy of phase approximation worse. This type of noise is usually the result of a combination of sensor thermal noise, quantum noise and film grain (if a film is used).

The probability distribution of the noise can be Gaussian, Poisson, a combination of these two or uniform. Also, the changes in the image induced by this type of noise are changing in time, as opposed to stationary noise types (pixel errors, salt and pepper noise), therefore simply subtracting a dark shot will not remove it (18). There are many known algorithms for getting rid of this noise type and several review papers are available (19; 20; 21).

The low-frequency noise types (gradual contrast or intensity changes) are usually harder to get rid of. Processes that lower the contribution of these corrupting effects are usually called ‘normalization’ processes. Instead of approaching the problem from the spectral side, as with the high-frequency type, algorithms aim to locally normalize the intensity and contrast of the image to balance the effects of this noise type. Difficulties arise when making global normalization routines local, as the local range of these filters are hard to approximate. It is very difficult to give a comprehensive list of publications that present local normalization algorithms, since the methods can be very different from local histogram-based methods (22) to model-based techniques (23) and mathematically more advanced and specific methods (24).

1.3.2 Extracting the Wrapped Phase

Until the second half of the eighties most methods for calculating the continuous phase map from two-dimensional interferometric images had been using extrema detection in the intensity image. In most cases locating continuous ridges and valleys in real intensity images alone incorporates interpolation. After the extrema are found, another interpolation step is needed to approximate the continuous phase surface between

ridges and valleys. Extrema detection-based methods have continued and continue to appear even recently (15; 25).

More sophisticated methods utilizing image transforms appeared in the late eighties. One example is the method published in (25) which uses the Fourier-transform to extract continuous phase information without extrema detection.

Equation [1] can be re-written by neglecting the high-frequency noise and carrier terms as

$$i(x,y) = a(x,y) + c(x,y) + c^*(x,y) \qquad [2]$$

with

$$c(x,y) = \frac{1}{2} b(x,y) \exp\left(j\psi(x,y)\right)$$

and $c^*(x,y)$ being the complex conjugate of $c(x,y)$ and j is $\sqrt{-1}$. Fourier-transformed, this gives

$$I(u,v) = A(u,v) + C(u,v) + C^*(u,v). \qquad [3]$$

Assuming that the frequency of the background intensity changes is much less than the frequency corresponding to fringe intensity periodicity, $C(u,v)$ and $C^*(u,v)$ will appear as two distinct peaks in the amplitude spectrum symmetrical to the origin. If one peak is

filtered from the amplitude spectrum, along with the zero-peak, the inverse transformed image will be complex valued and the interference phase can be demodulated as

$$\psi(x,y) = atan\left[\frac{Im\big(c'(x,y)\big)}{Re\big(c'(x,y)\big)}\right]. \quad [4]$$

where *c'(x,y)* means the inverse transformed complex image. Note that due to the inverse tangent function, this demodulated phase will be in a modulo 2π form. The filtering of either *C(u,v)* or $C^*(u,v)$ is not an obvious process. The simplest filter to use is a band-pass filter cutting any of the four half-planes. The use of such a filter is described in (25), concluding that even if one uses both half-planes to extract phase information, the method will still fail for a number of more complicated images. More sophisticated filtering procedures are described in (26; 27). Hilbert and Schlieren transforms can be used to generalize the above formulation. A method using this more general approach is described in (28). This method is further used in this work and is described in detail in section 2.3.2.

1.3.3 Unwrapping the Modulo 2π Phase

Formally, the unwrapping problem can be described by the following equation:

$$\Psi(x,y) = \psi(x,y) + m(x,y)2\pi \quad [5]$$

where *m(x,y)* is a matrix of integers, therefore the wrap count *m(x,y)* is a function that aims to remove the 2π discontinuities in the wrapped phase map $\psi(x,y)$. Thus, the

unwrapping problem is to find such an $m(x,y)$ that produces a physically meaningful continuous phase map $\Psi(x,y)$. The term "physically meaningful" refers to the fact that the phase extraction problem very rarely has a unique solution. The reason for this is that the absolute phase representing the absolute optical path length difference of the two beams cannot be measured directly, because fringe orders are indistinguishable based on intensity information alone. Therefore additional constraints must be introduced to the fringe processing step in order to narrow down the set of possible solutions to find the physically meaningful continuous phase map. One can already see that this is easier when imaging closed fringe formations, if every fringe caused by the studied optical inhomogeneity is contained in the image, as in the case of studying perturbed transparent media, but is impossible in the case of techniques utilizing carrier frequencies, as in the case of surface roughness measurements. In the case of these applications, the first deformed fringes indicate the boundary of the region of interest.

The first formal derivation of an unwrapping algorithm has been published by Kazuyoshi Itoh in an 1982 Applied Optics letter (29). Itoh studied the phase unwrapping problem motivated by formalizing the methodology that had been used in meteorological measurements. The short study concluded that the unwrapped phase can be obtained by differentiating, wrapping and integrating the original sequence (which is practically the wrapped phase signal). Formally, this can be written as

$$s(m) = s(0) + \sum_{n=1}^{m} \Phi_2 \Delta \Phi_1 \mathrm{s(n)}, \qquad [6]$$

where Φ_i is the wrapping operator satisfying the following relationships:

$$\Phi_i s(n) = s(n) + 2\pi k_i(n), \quad [7]$$

where *s(n)* is a sequence of complex arguments and k_i is a sequence of integers such that

$$-\pi \leq \Phi_i s(n) < \pi \quad [8]$$

and Δ is the discrete differentiation operator. It can be seen intuitively that equation [6] simply tells that if one cumulatively adds the differences in the wrapped signal to the 'initial' signal *s(0)* then the continuous phase signal will be recovered provided that the differentiated sequence is wrapped appropriately. Itoh's algorithm holds for two-dimensional phase maps as well, but errors due to discontinuities or local phase errors will be propagated all through the signal. A strategy for finding the optimal path for integration has also to be found.

The next generation of phase unwrapping algorithms focused on finding an optimal integration path so that no global errors are generated due to local error propagation. Goldstein's work published Radio Science in 1988 was the first of many papers discussing and perfecting this approach (30). These methods are collectively called 'branch cut' algorithms, as the path seeking algorithm is heavily based on network search routines developed in the area of artificial intelligence. The term branch cut refers to blocking points in the wrapped phase map which produce discontinuities so that no integration path can cross it and propagate the error. A variation of this technique can be achieved by introducing weighting factors for discontinuities based on initial phase image

quality. This allows the unwrapping overlaying image regions (where phase discontinuity is not an error caused by noise or quantization) without penalty, but does not allow local error propagation due to noise. Such an algorithm has been described by Flynn in 1997 and has been referred to as ‘Flynn’s minimum discontinuity’ method since then (31). Since this algorithm is used in this thesis, it is described in detail in section 2.3.4.

Although phase unwrapping algorithms based on branch cut are considered as the best available algorithms in terms of accuracy (32), other methods based on entirely different approaches are also available. The works of Ghiglia et al. are worth mentioning (33; 34), introducing cellular automata and least-square methods for phase unwrapping. Another least-square method utilizing a multigrid technique for multi-scale phase approximation is used in this thesis and is described in detail in section 2.3.3 (17).

Regularized least-square methods followed the work of Ghiglia et al. Regularization is a term that refers to a mathematical method in which additional a priori information is introduced to solve ill-posed problems, such as the phase unwrapping problem. In practice, regularization usually introduces cost functionals to penalize or promote different options in the unwrapping algorithm so that the most ‘meaningful’ result is obtained. The term ‘meaningful’ refers to additional information coming from physical understanding which restricts the solution to certain conditions. Such a condition can be the continuity or smoothness of the unwrapped phase map. Algorithms using the regularized approach are presented in (35; 36).

1.4 Validation and Uncertainty Quantification

Validation and uncertainty quantification (V/UQ) plays an increasingly important role in the research of scientific computing as the sophistication of simulations increase. The area of V/UQ is often considered as not an exact field of mathematics but a subjective collection of suggested frameworks and techniques for approximating or predicting uncertainties of scientific computations. Books and thorough review articles are available in this area (37; 38). Here I follow the condensed nomenclature and discussion of Roy and Oberkampf (39).

The term ‘validation’ means the “assessment of model accuracy by way of comparison of simulation results with experimental measurements” (39). Validation has two roles: first, it statistically quantifies the disagreements between experimental and simulation data and second, it extrapolates the uncertainties to domains where experimental data for comparison is not available. Confidence intervals (parameter ranges in which the prediction is considered valid) are also extrapolated. To carry out this assessment, one must quantify all uncertainties arising either on the experimental or computational side.

Uncertainties are generally considered to appear in two forms: aleatory and epistemic uncertainties. Aleatory uncertainties are also called stochastic uncertainties or variations. The cause of aleatory uncertainty is the inherent variation and randomness in sampled populations. Aleatory uncertainty can be treated statistically as probability density functions (PDFs) or cumulative distribution functions (CDFs). Epistemic uncertainties are also called reducible or ignorance uncertainties. The cause of this type of uncertainty is the lack of knowledge on the part of the analyst or experimentalist. In theory, epistemic

uncertainty can be completely eliminated by adding more information or insight to the process of validation. Mathematically epistemic uncertainty can be treated as an interval with no associated PDF or as statistical variables with uniform PDFs. Undersampled aleatory uncertainties can also be handled as epistemic uncertainties, because the insufficient number of samples represents lacking information.

In computational models, uncertainties can come from a number of different sources. The model inputs may take uncertain forms represented by either known or unknown PDFs. Uncertainties arise due to numerical approximations of continuous variables (the validation of this type of uncertainties only is called ‘verification’ by some authors (39)). Computational models usually also contain many physical assumptions that introduce additional uncertainties into the predictions of the model.

The framework suggested by Roy and Oberkampf consists of a number of steps:

- The identification of all sources of uncertainty. One must identify the above mentioned types of uncertainties in the model inputs, model assumptions and numerical approximations.
- The characterization of uncertainties. Mathematical structures must be assigned to the identified uncertainties and they must be quantified numerically.
- The propagation of input uncertainties through the model.
- The estimation of model form uncertainty. Model form uncertainty is evaluated with the help of validation metrics. A validation metric is usually a scalar that describes the quality of agreement between the model and

experiment. Validation metrics can be defined in many different ways and choosing one definition will dictate further steps in analysis.

– The determination of the total uncertainty in the system response quantities. A number of things can be done in this step. First, the propagated uncertainties can be summed and the total uncertainty in the system response quantities of interest can be computed. Second, based on the estimated model and experimental uncertainties, feasible regions can be constructed where the model predictions are consistent with the experimental results. Finding consistent ranges in the system response space may reduce the uncertainty ranges of the model predictions, leading to information gain in the validity of the model predictions (38).

Other authors suggest similar frameworks for computational model validation and uncertainty quantification, but as stated above, methods are rarely exact mathematically. Therefore a number of accepted techniques exist for model validation and uncertainty quantification and it is important to describe the used methodology in each study. A detailed description of the method used in this thesis is described in section 2.4.2.

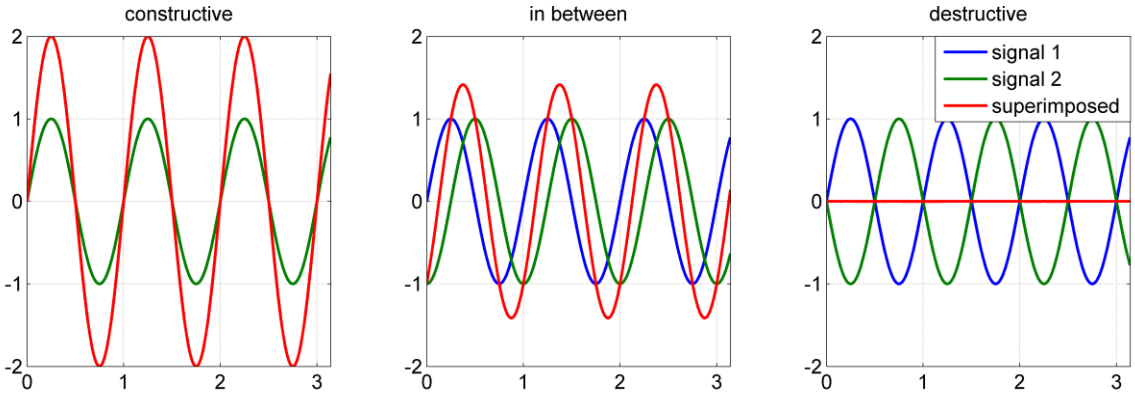

Figure 1: Illustrating constructive and destructive interference

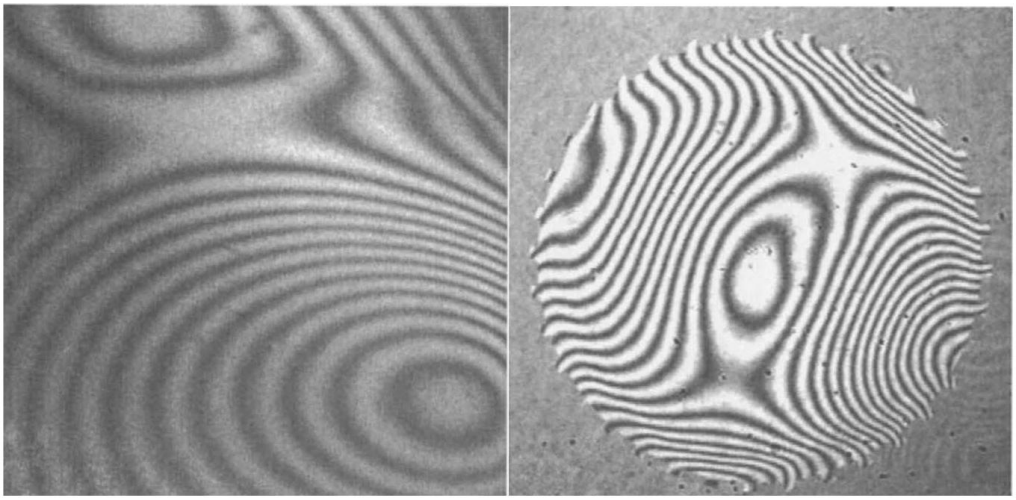

Figure 2: Typical fringe patterns from holographic interferometry

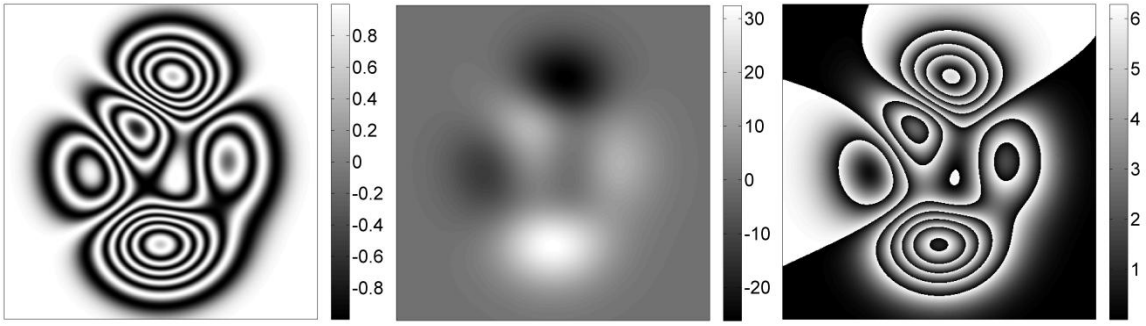

Figure 3: Simulated ideal fringe pattern and the underlying phase. Left: fringe pattern; middle: underlying continuous phase; right: underlying wrapped phase

CHAPTER 2

METHODOLOGY

In this chapter, the methodology used in the actual validation work is described in detail. In brief, our methodology consists of the following main steps:

- Obtaining the interferometric images by carrying out the plume experiments.
- Carrying out the plume simulations.
- Processing the interferometric images to extract continuous phase information. This step consists of the following steps:
    - Preprocessing, registration and filtering of the intensity images.
    - Extracting the wrapped phase maps by using the isotropic quadrature transform technique.
    - Unwrapping the wrapped phase maps by using the weighted multigrid method and the minimum discontinuity method. Later, the performances of the two techniques are evaluated in terms of consistency.
    - The postprocessing of continuous phase maps in order to be able to compare them with the simulation data.
- The processing of the obtained consistency dataset.

2.1 The Helium Plume Experiment

The original experiments were developed and carried out by Schönbucher et al. in Germany, 1984 at the University of Stuttgart (40). The recorded images were digitized 15 years later by IWF - Wissen und Medien gGmbH.

2.1.1 The Experimental Setup

A schematic of the experimental setup of Schönbucher et al. is shown in Figure 4.

The group performed four experiments. In each experiment, helium was flowing through a circular outlet with a diameter of 50 mm. The flow rates of the helium was varied between 2 and $2.5 \cdot 10^{-4}$ m^3/s (2.25, 2.0, 2.5 and $2.3 \cdot 10^{-4}$ m^3/s, respectively). Temperature and pressure measurements have not been carried out to the best of our knowledge, therefore these have been estimated based on local historical weather data.

To create the interferometric images, the beam of a continuous 2 W argon laser with a wavelength of 514.5 nm was split into measurement and reference beams as discussed in section 1.2.1. The measurement beam was reflected through the transparent helium plume while the reference beam was passed through quiescent air. The two beams were re-united on a holographic plate and the formed interferometric images were captured by a high-speed camera at a frame rate of 1000 frames per second.

2.1.2 The Acquired Images

The digitized images were acquired by scanning the originally obtained photographs. The scanned images are all 1980 by 1080 pixel size, 24 bit RGB images. A typical interferometric image is shown in Figure 5. The plume boundaries can be determined by

locating the first significant changes in the gradient image on both sides. However, the exact location of these boundaries is usually hard to find from interferograms alone.

Approximately 2500 images were digitized in each experimental set. As it is apparent from Figure 5, the overlapping region defined by the two beams did not cover the whole lower region of the plume; therefore the fringes in the lower region of the image are discontinuous and are not connected to the contour of the outlet. The alignment of the 'scene' also varies in different images due to the manual method of digitization. The images were stored as .tif files.

The quality of the images is not very high. Apart from high-frequency photonic noise, lower frequency degenerative effects are also present caused by the imperfections of the imaging media that had been used in the original experiment. Fringe-like objects are visible outside the assumed plume boundary in some images. This suggests impurities in the air in the room where the experiments were carried out.

2.2 Helium Plume Simulation

The helium plume simulations have been carried out by Weston Eldredge at the University of Utah and reported in 2011 (41). A schematic showing the main characteristics of these simulations are shown in Figure 6.

The modeled volume was a 13.8 cm^3 cube. The helium inlet was placed at the center of the bottom plane. The bottom plane itself acted as an air inlet, simulating the air co-flow phenomenon often arising when dealing with buoyancy driven problems. The four sides of the simulation domain acted as pressure boundary conditions and the top plane was an outlet boundary. Each simulation was run for 6 seconds of simulated time. The

velocities for helium and air were constant for the whole simulated time range. A total number of 100^3 uniformly placed nodes were used.

The CFD engine used for the simulations was ARCHES, a LES-based engine for modeling turbulent flames. ARCHES has been modified in order to be able model laminar cases. To model the mixing of helium and air in each node, a constant-coefficient Smagorinsky model was used. To provide laminar diffusivities to compute mixing, the Schmidt number for each node was computed. To obtain the Schmidt number, the fluid viscosities and binary diffusivities must be estimated. The former was approximated by a polynomial fit on the data of Incropera and Dewitt (42) and using the method of Reichenberg (43) to estimate the mixture viscosities. The binary diffusivities of the air/helium system were approximated by using the method of Wilke and Lee (44).

The output uncertainty ranges were determined by introducing input uncertainties to the model. Three active variables have been chosen, the helium inlet velocity, the air inlet velocity and the system temperature. For more information on output uncertainty quantification, please refer to section 2.4.1. The nominal value for the helium inlet velocity has been chosen to be 0.135 m/s, the nominal velocity for the air inflow has been chosen to be 0.0405 m/s and the nominal system temperature was 315.15 K. Temperature and pressure data have been chosen based on historical local weather data.

Among others, the simulations yielded numerical concentration fields x_{He} as a result. These have been converted to phase fields by applying the following formula:

$$\psi_{x,y} = \frac{2\pi s_{x,y}}{\lambda} |n_{air} - n_{mixture}|_{x,y} = \frac{2\pi s_{x,y}}{\lambda} (x_{He} |n_{air} - n_{He}|)_{x,y} \quad [9]$$

where $\psi_{x,y}$ is the continuous phase map, $s_{x,y}$ is the the length of the path that the light travels inside the plume, λ is the wavelength of the light and n is the refractive index. Subscripts x,y indicate that the fields are two-dimensional and discrete. Thus three-dimensional concentration data is converted into projected two-dimensional phase data by the use of equation [9].

2.3 Fringe Pattern Analysis

In this section a detailed description of our image processing methodology is given. The procedure can be divided into four steps, namely: pre-processing, phase demodulation, phase unwrapping and post-processing. The ultimate purpose of these steps is to effectively and accurately extract phase information from whole image sets in an automated way that can be compared to simulation data or can be the input of consistency analysis and V/UQ.

2.3.1 Preprocessing

The role of preprocessing is two-fold. First, it enables further processing and makes data extraction the most effective by filtering or transforming the image. Second, in the case of the helium plume images an additional preprocessing step called ‘registration’ was necessary to reduce the errors caused by manual digitization.

Since we have used relatively noise-immune algorithms for phase demodulation and unwrapping, prefiltering and de-noising were not as important as they typically are. However, in some cases the unwrapped phase output was sensitive to pixel variations in the original intensity images due to the ambiguity in global continuous phase solutions as

mentioned earlier in section 1.3.3. In these cases, small discontinuities or insufficient resolution in the initial images lead to unstable unwrapping. Typical phase profiles are expected to have one global maximum at the centerline of the plume, since the phase difference of the two beams will be the highest at this location; however, phase discontinuities at the center of the plume can cause the unwrapping algorithm to produce significantly different results, e.g., monotonically increasing or decreasing phase profiles or profiles with multiple maxima. In these cases it was necessary to perturb the intensity images in a way that it does not alter the continuous phase profile significantly compared to the expected, physically meaningful result, but changes the pixel values so that a 'right' solution can be obtained. This approach exploits the sensitivity of the unwrapping algorithms to small discontinuities in terms of obtaining the physically meaningful global solution that sometimes occurred. Filtering is a good way to achieve this small perturbation in pixel values in the intensity images, because at the same time it can reduce noise levels and filters can be set up in way so that they do not alter the fringe patterns too much. For this purpose, generalized spin filters were used, because they achieve noise-reduction and leave the fringe skeleton unchanged. Spin filters are practically local averaging filters, but the local windows are defined in a way so that the averaging happens along paths parallel to local fringe orientation. In this way, the loss in phase data is minimized, because no fringes disappear or get blurred by the filter (45). The algorithm determined whether additional attempts are needed to produce the physically meaningful solution by cross-correlating the actual normalized phase profile *np* with a previously obtained averaged 'standard' phase profile. Normalized phase profiles are defined as vectors of the column averages in the discrete phase map with

values normalized between 0 and 1. Since the plume images were sufficiently large in the vertical direction, this averaging seemed to always produce approximately the same profile for all the images. A crisp threshold value of 0.8 was defined as the lowest limit of acceptable correlation strength between the actual and standard profiles. If the actual phase map did not meet this requirement, additional attempts were made in order to reach a meaningful solution. If the threshold value was not exceeded, the new attempt would be made with applying the spin filter to the image. For even more degraded images, varying the demodulation parameters was necessary. Section 2.3.5 presents details about this process. Figure 7 demonstrates the unwrapping instability problem.

Registration, as mentioned in section 2.3.1, is a procedure that is required if the images do not have the same global coordinate system. Registration has also been carried out in an automated way by exploiting the fact that the laser ‘spots’ did not move relative to the plume during an experiment. As can be seen in Figure 5, the outer spot can be detected easily, since the background of the images was very dark compared to the illuminated areas. Once the spot was detected in an image, the coordinates of its perimeter pixels were found by applying morphological operations and computing the difference of the eroded and dilated image. A circle was fit on the perimeter pixels and the center of this circle was used to find the global coordinate system between the images. The circle was fit by minimizing the sum of squared radial deviations. Figure 8 demonstrates the registration process.

2.3.2 Phase Demodulation by an n-Dimensional Quadrature Transform

The method that we used to demodulate the acquired interferograms was published by Servin et al. in the Journal of the Optical Society of America in 2003 (28). The basic idea of their method is to find the quadrature of the obtained n-dimensional interferometric signal, because knowing the quadrature signal closes the inverse problem of finding the phase angle $\Psi(x_1,x_2 \ldots x_n)$ from the n-dimensional cosine signal of an intensity image. Thus their method is practically a numerical method to obtain a *–sin* form of the originally *cos* form signal.

The n-dimensional quadrature operator is defined as

$$Q_n[b(\boldsymbol{r})\cos(\psi(\boldsymbol{r}))] = -b(\boldsymbol{r})\sin(\psi(\boldsymbol{r})) \qquad [10]$$

where Q_n is the quadrature operator and $\boldsymbol{r}$ is the vector of coordinates. The quadrature is computed by calculating the gradient of the intensity image

$$\nabla I(\boldsymbol{r}) = \cos\big(\psi(\boldsymbol{r})\big)\nabla b(\boldsymbol{r}) + b(\boldsymbol{r})\nabla[\cos(\psi(\boldsymbol{r}))] \qquad [11]$$

In most cases, the first term of equation [11] can be neglected, because the intensity variation term b(r) is usually a low-frequency term. Applying the chain rule to the second term we obtain

$$\nabla I(\boldsymbol{r}) = -b(\boldsymbol{r})\sin\big(\psi(\boldsymbol{r})\big)\,\nabla\psi(\boldsymbol{r}) \qquad [12]$$

If the local sign and frequency of $\nabla\psi(r)$ is known, the quadrature signal can be obtained by the following:

$$Q_n[b(\boldsymbol{r})\cos(\psi(\boldsymbol{r}))] = -b(\boldsymbol{r})\sin(\psi(\boldsymbol{r})) = \frac{\nabla\psi(\mathbf{r})}{|\nabla\psi(\mathbf{r})|^2}\cdot\nabla\mathrm{I}(\mathbf{r}) \qquad [13]$$

ergo dividing the product of the gradients of the intensity image and modulating phase by the squared magnitude of the modulating phase. However, $\nabla\psi(r)$ cannot be computed directly from $I(r)$ in the most cases. Equation [13] can be rewritten as

$$Q_n\big[b(\boldsymbol{r})\cos\big(\psi(\boldsymbol{r})\big)\big] = -b(\boldsymbol{r})\sin\big(\psi(\boldsymbol{r})\big) = \frac{\nabla\psi(\mathbf{r})}{|\nabla\psi(\mathbf{r})|}\cdot\frac{\nabla\mathrm{I}(\mathbf{r})}{|\nabla\psi(\mathbf{r})|} = \qquad [14]$$
$$= \mathbf{n}_{\boldsymbol{\phi}}\cdot\frac{\nabla\mathrm{I}(\mathrm{r})}{|\nabla\psi(\mathrm{r})|}$$

where $\boldsymbol{n_\phi}$ is a unit vector normal to the local isophase contour, in other words, the n-dimensional local fringe orientation vector. The task then is to find the vector fields $\boldsymbol{n_\phi}$ and $\nabla I/\nabla\Psi$.

Since the vector field $\boldsymbol{n_\phi}$means the orientation field of the original intensity image, it is easy to obtain from the gradient image, provided that the image is normalized, i.e. the local variation in pixel values are the same at every point of the image. For normalization we have used an algorithm published by Guerrero et al. developed specifically for interferogram demodulation (46). Once the intensity image is normalized, the local orientation angle can be obtained as

$$\theta(x,y) = \operatorname{atan}\left[\frac{\partial I(x,y)/\partial y}{\partial I(x,y)/\partial x}\right] \qquad [15]$$

Unfortunately, the obtained orientation angles will be wrapped between values 0 and π due to the *atan* operator. The orientation angle values can be unwrapped by arbitrarily choosing a sign in one location and adjusting the rest. After the orientation angles are computed, the vector field $\boldsymbol{n_\phi}$ can be set up given that its magnitude is unity in every point.

For the calculation of the vector field $\nabla I/\nabla \Psi$ Servin et al. proposes a method based on the Fourier transformation. They compute the generalized Hilbert transform of the image by the following:

$$H_2[I(x,y)] = \mathcal{F}^{-1}\left[\frac{\mathcal{F}(\nabla I(x,y))}{\sqrt{u^2+v^2}}\right] \approx \frac{\nabla \mathrm{I}(\mathbf{r})}{|\nabla \psi(\mathbf{r})|} \qquad [16]$$

where *F* is the Fourier transformation operator, F^{-1} is the inverse Fourier transformation and *(u,v)* is the Fourier transform space of the $\boldsymbol{R}^2$ = *(x,y)* plane.

Phase demodulation by this method may seem an exact procedure. Indeed, the extraction of $\nabla I/\nabla \Psi$ might be considered exact if several assumptions hold. However, the extraction of the vector field $\boldsymbol{n_\phi}$ in the modulo 2π form requires mathematical regularization in order to avoid sharp jumps in the orientation angle field caused by the ambiguity of the orientation sign. Servin et al. suggest the use of a cost-function based

regularization technique published by Villa et al. (13). This method sets up a cost function

$$U_r(\boldsymbol{n}) = \sum_{\tilde{\boldsymbol{r}} \in (\Gamma \cap L)} [m(\tilde{\boldsymbol{r}}) \cdot n(\boldsymbol{r})]^2 + \mu[n_x(\boldsymbol{r}) - n_x(\tilde{\boldsymbol{r}})]^2 s(\tilde{\boldsymbol{r}}) + \mu\left[n_y(\boldsymbol{r}) - n_y(\tilde{\boldsymbol{r}})\right]^2 s(\tilde{\boldsymbol{r}}) \quad [17]$$

where $\hat{\boldsymbol{r}}$ denotes the neighborhood of the location $\boldsymbol{r}$ in the orientation field, μ is the regularization parameter, Γ is the neighborhood size and $s(\boldsymbol{r})$ is a Boolean value which is one if a given location has already been regularized. Villa et al. present a method to minimize this cost function in order to extract the smoothest possible orientation map modulo 2π. From this description it is easy to see that the demodulation algorithm employing this regularization technique is also controlled by these two parameters. As described in section 2.3.1, when unwrapping instability occurred, our strategy was to vary these parameters in order to obtain a physically reasonable unwrapped solution.

2.3.3 Phase Unwrapping by the Weighted Multigrid Method (PUWM)

This method is one of the two algorithms that we used to unwrap the demodulated phase maps. For a comparison of the performance of the two in terms of consistency with simulation data, please refer to section 3.4. The PUWM method was published by Mark D. Pritt in IEEE Transaction on Geoscience and Remote Sensing in 1996 (17).

PUWM is a weighted least-squares unwrapping algorithm which utilizes multigrid extensions of the Gauss-Seidel relaxation technique. The principle of least-squares unwrapping is to find a continuous phase solution that minimizes the differences between

the gradient of the wrapped phase map and the gradient of the unwrapped phase map. The partial derivatives are defined in the discrete case as follows:

$$\Delta_{ij}^{x} = \psi_{ij} - \psi_{i-1,j} \text{ and } \Delta_{ij}^{y} = \psi_{ij} - \psi_{i,j-1} \quad [18]$$

where the discrete differentials exceed π, 2π is added or subtracted to the differential. This ensures that the smoothness of the phase map is conserved and corrects the differentials in the case of the wrapped map. Computing the differences between the wrapped and unwrapped phase maps leads to the Laplace equation in the following way:

$$\sum_{i,j}\left(\Psi_{ij} - \psi_{i-1,j} - \Delta_{ij}^{x}\right)^2 + \sum_{i,j}\left(\Psi_{ij} - \psi_{i,j-1} - \Delta_{ij}^{y}\right)^2 = 0 \quad [19]$$

$$\left(\Psi_{i+1,j} - 2\psi_{ij} + \Psi_{i-1,j}\right) + \left(\Psi_{i,j+1} - 2\psi_{ij} + \Psi_{i,j-1}\right) = \rho_{ij} \quad [20]$$

where ρ_{ij} is the Laplacian of the phase.

It is easy to see that this particular way of posing the unwrapping problem leads to the equation of Laplace, $\nabla^2 \Psi = \rho$, which can be written as a linear system:

$$A\Psi = \rho \quad [21]$$

which can be solved by the method called Gauss-Seidel relaxation. The disadvantage of this method when applied to phase unwrapping is that it tends to unwrap through phase discontinuities rather than around them, which leads to unwanted error propagation. To

overcome this problem, the least-squared method can be extended as the weighted least-squares method:

$$\sum_{i,j} \omega_{ij}^{x}\left(\Psi_{ij} - \psi_{i-1,j} - \Delta_{ij}^{x}\right)^2 + \sum_{i,j} \omega_{ij}^{y}\left(\Psi_{ij} - \psi_{i,j-1} - \Delta_{ij}^{y}\right)^2 = 0 \qquad [22]$$

The weighting factor w can be defined and determined prior to unwrapping attempts in many different ways. The approach we took in this work is to define it as the local reliability of the orientation vector field approximation by the quadrature transform method. This approach ensures that reliable data points in the wrapped phase map will contribute more to the unwrapping solution than inconsistent regions.

The weighted least-squares method is further improved by introducing multigrid concepts to the algorithm. Multigrid methods are techniques to solve partial differential equations (PDEs) on large grids. They work by iteratively passing the solution between coarser and finer grids, repetitively applying the relaxation method. Multigrid techniques are generally as fast as direct Fourier-transform methods but are applicable to more complex problems like nonlinear PDEs as well. The implemented method utilizes the so called V-cycle multigrid approach, which sweeps through grid levels backwards and forwards until convergence is reached. There are no additional parameters to this algorithm, except the reliability field for weighted least-squares.

2.3.4 Flynn's minimum weighted discontinuity method (PUMD)

The performance of this algorithm is compared to the performance of the weighted multigrid method in terms of consistency with simulation data in section 3.4. This

algorithm was published by Thomas J. Flynn in the Journal of the Optical Society of America in 1997 (31).

PUMD is similar to PUWM. The only difference – apart from algorithm implementation – is how it defines the cost function to be minimized by the solution. Given that we seek the smoothest possible solution, it is practical to define the vertical and horizontal jump count functions q_{ij} and z_{ij} as

$$q_{ij} = \left\lfloor \frac{\Psi_{ij} - \Psi_{i-1,j} + \pi}{2\pi} \right\rfloor \quad [23]$$

$$z_{ij} = \left\lfloor \frac{\Psi_{ij} - \Psi_{i,j-1} + \pi}{2\pi} \right\rfloor \quad [24]$$

where the brackets mean the floor function. Therefore, if the difference between the two adjacent phase values is larger than π, the jump count is equal to 1. If we apply equation [5], we can express the jump counts as functions of wrap counts and the wrapped phase image:

$$q_{ij} = m_{ij} - m_{i-1,j} + \left\lfloor \frac{\psi_{ij} - \psi_{i-1,j} + \pi}{2\pi} \right\rfloor \quad [25]$$

$$z_{ij} = m_{ij} - m_{i,j-1} + \left\lfloor \frac{\psi_{ij} - \psi_{i-1,j} + \pi}{2\pi} \right\rfloor \quad [26]$$

PUMD aims to find m_{ij} by minimizing the sum of the magnitudes of the jump counts $E_0(m, \psi)$:

$$E_0(m,\psi) = \sum_{(i,j)\in Q} |q_{ij}| + \sum_{(i,j)\in Z} |z_{ij}| \quad [27]$$

An unwrapping solution is called a minimum discontinuity solution if it gives the minimum of $E_0(m,\psi)$ over all choices of m.

For the same reason as in the case of PUWM, it is important to introduce weighting factors for the cost function. Therefore the weighted minimum discontinuity method will use the following cost function:

$$E_0(m,\psi) = \sum_{(i,j)\in Q} \omega_{ij}^{x}|q_{ij}| + \sum_{(i,j)\in Z} \omega_{ij}^{y}|z_{ij}| \quad [28]$$

Again, the weighting factors are chosen based on phase data reliability.

2.3.5 Postprocessing

The purpose of postprocessing was to convert the extracted unwrapped phase maps into a form that can be the input of the consistency analysis routines. The first problem was to extract discrete phase matrices that have the same global coordinate system and spatial resolution as the simulation results. This step was necessary because the spatial resolution of the simulated matrices were determined by the coarseness of the numerical grid. This was 100^3 in all cases in a 13.8×13.8×13.8 cm^3 modeled volume. This three-dimensional spatial resolution lead to a 100×100 node projected resolution. The resolution of the experiments was much higher than this and it was mainly determined by the resolution of the images. Since the image sizes were 1920×1080 pixels with an

'active' area of approximately 1000×1000 pixels. Therefore, a reduction of one order of magnitude was necessary to be able to compare the results. This was done by locating the central positions of simulation nodes in the images using the global coordinate system that was set up by the registration routine as mentioned in section 2.3.1 and averaging around these points in an area that corresponded to one differential volume in the CFD model.

Some difficulties arose after the unwrapping step as well. The previously mentioned unwrapping instability phenomenon often presented itself in a typical way. In these cases, the number of extrema in the normalized phase profiles were correctly one along the centerline of the plume, however instead of finding one maximum, the algorithm found one minimum at the same location. This is a typical result of the ambiguity and under-determination of the phase unwrapping problem, as there is insufficient information to determine whether a modulating physical phase map with a single maximum or a single minimum caused the resulting fringe pattern. In these cases, the unwrapped phase map was simply 'inverted', i.e., the new phase map was determined by the following equation:

$$\Psi_{\mathrm{inverted,ij}} = \max\left(\Psi_{\mathrm{ij}}\right) - \Psi_{\mathrm{ij}} + \min\left(\Psi_{\mathrm{ij}}\right) \qquad [29]$$

This simple procedure converted the single minimum into a single maximum.

Another postprocessing step was the re-scaling and shifting to zero of extracted phase maps. Again, the absolute continuous phase map is impossible to calculate from single fringe images without any spatial or temporal carrier or phase-shifting techniques (the problem is detailed in section 1.3.3). Therefore, the unwrapping algorithms produced

continuous phase maps which satisfied their optimization criteria but these were rarely meaningful physically in the absolute sense. For example, a constraint coming from physical intuition is that the phase must be close to zero at the plume boundaries, because at those locations, there is no perturbation in the optical medium that would explain phase changes. Thus, the unwrapping process only produced the correct gradients of the absolute phase maps, not the correct absolute values. By introducing physical constraints and boundary conditions, the phase maps were re-scaled and shifted so that they satisfied the boundary conditions.

2.4 Uncertainty Quantification

In this section a detailed description of the procedure for the estimation of experimental errors and uncertainty and the method for quantifying consistency with simulation data is given.

2.4.1 Estimation of Experimental Errors

The main source of bias errors (a systematic form of epistemic uncertainty) is the falsely detected fringes in the holographs. The applied algorithms tend to identify background noise and inhomogeneous illumination as fringes or miss fringes that are parts of dense patterns. The former phenomenon causes a systematic over-prediction, while the latter leads to a systematic under-prediction in the phase field.

These errors were estimated by the following method. The demodulated and unwrapped phase maps were available from previous calculations for all frames in every experimental set. The original fringe pattern can be re-obtained from these maps by

simply taking the cosine of the unwrapped maps. The re-obtained fringe patterns can then be compared to the very original images to see if the algorithms created or destroyed any fringes in the process.

Because the density of the fringe pattern in this case is mostly a function of the vertical coordinate Y, we have calculated the re-obtained fringe patterns of several images and manually computed the errors in fringe numbers at different heights. These errors can be transformed to errors in Ψ values by simply multiplying by 2π, because a fringe pattern with one missing or falsely identified additional fringe will always have a $\pm 2\pi$ error in Ψ at most. Figure 9 shows the averaged systematic error in Ψ as a function of the vertical coordinate *y* in the plume.

The correctness of these bias error values have been checked by computing the concentration of helium at the bottom of the plume in its centerline. Here the calculated concentration should be very close to 100% helium. The computed concentration values always got closer to 100% by subtracting the bias error at that height in the plume. The residuals were smaller than 0.005 (mole fraction).

The main source of the random errors (aleatory uncertainty) is the uncertainty in instantaneous Ψ values caused by the empirically chosen algorithm input parameters Γ and μ. The former is the neighborhood size, which determines the area around locally chosen pixels in which the calculation proceeds. The higher the value of Γ, the more accurate the demodulation is, because fringes that are further away from the local region of interest also contribute to the result. The second parameter is the vector regularization parameter. This is a parameter controlling the smoothing of the local orientation vectors, which are used by the demodulation process to determine the direction for integration.

The random errors have been approximated by a second order sensitivity analysis of these input arguments. The total errors have been computed by using error propagation. Because of the same reasons as described above, the magnitude of the random error is also a function of the vertical coordinate. Figure 10 shows the magnitude of the random error as a function of height. Because the unwrapping algorithms did not have any independently variable parameters, the random errors have been estimated by analyzing the sensitivity of the demodulating algorithm only.

After the bias and random errors have been quantified, the mean bias error has been subtracted from the phase data. Two-dimensional matrices have been created and filled with the values from the mean bias error profile, assuming constant bias error at a given height. After subtraction, the translated phase data have been assigned an experimental uncertainty equal to the sum of the random error and the temporal standard deviation of the bias error profile.

2.4.2 Consistency Analysis

Pairwise consistency tests have been carried out between the experimental and simulation datasets. Since the spatial resolution of the experimental data was higher, the experimental results have been downgraded to match the spatial resolution of the simulation dataset (for details, see section 2.3.5). The temporal resolution of the simulations was higher, but since both the simulations and the experiments had been designed in a way so that many ‘puff cycles’ can be recorded or simulated in one case, the time-averaged results should converge to a consistent result. At the current state of

the project, only the time-averaged (mean) phase maps have been checked for consistency.

Pairwise consistency tests provide information about whether the model (simulation) and the experiment are consistent at certain spatiotemporal locations in the datasets. To understand concepts in consistency analysis, one has to define a dataset unit Y_i:

$$Y_i\{y_i, u_i, l_i, y_m(\boldsymbol{x})\}$$

where y_i is the experimental measurement with lower and upper bounds l_i and u_i, respectively and $y_m(\boldsymbol{x})$ is a model prediction with a vector of input parameters $\boldsymbol{x}$.

A dataset Y is considered consistent if the following condition is satisfied:

$$\forall\, i:\ u_i \geq |y_m(\boldsymbol{x}) - y_i| \geq l_i$$

A pairwise consistency test is repeated for every combination of two dataset units. Ergo many datasets are constructed, each containing a given combination of two dataset units. With temporally averaged, spatially nonuniform data, every combination means every combination of sampled spatial locations.

Even if a dataset is inconsistent, it is practical to define a scalar called the *consistency measure*. A consistency measure is defined in a way so that its value tells one how consistent or inconsistent the dataset is. Here we denote the consistency measure as γ and define it in the following way (47):

$$\forall\, i : (1-\gamma)u_i \geq |y_m(\boldsymbol{x}) - y_i| \geq l_i(1-\gamma)$$

$$\beta_j \geq x_j \geq \alpha_j$$

By this definition, the consistency measure is a scalar that is the minimum value of γ with which the dataset is still consistent at the best choice of $\boldsymbol{x}$ inside its variation bounds $\boldsymbol{\beta}$ and $\boldsymbol{\alpha}$. It is easy to see that if $\gamma = 1$, the experimental bounds can be reduced to total certainty, which means that the two nominal values (experimental measurement and model prediction) are exactly the same. The consistency measure must be above zero for a dataset unit to be considered as consistent.

Pairwise consistency maps can be prepared by computing the consistency measure for every combination of dataset units. Consistency maps are checkerboard plots with color-coded values of the consistency measure. They contain *k* rows and columns, producing all possible combinations of dataset-doublets. In the diagonal of the consistency map the datasets contain only one dataset unit (or two times the same dataset unit). If a dataset unit is not consistent with itself, it will not be consistent with any other dataset units.

The pairwise consistency tests have been carried out by only looking at horizontal profiles in the time-averaged phase data at different heights in the plume. Therefore the dataset units were the discrete locations in the one-dimensional profiles.

Three different levels of assumptions have been tested. First, the experimental and simulation data have been compared by only introducing the above described uncertainty sources. The second level was assuming an axially symmetrical experimental plume and considering any deviations from an axially symmetric pattern as uncertainty. We argue that this is a logical step because the simulated cases were all axially symmetric and

therefore an experiment is needed for validation that also yields axially symmetric plumes. The contribution and magnitudes of physical effects that may cause the plume to deviate from the axially symmetric pattern are unknown and thus should be treated as experimental uncertainty. In this case, the phase profiles have been converted into symmetrical profiles. The symmetrical nominal values have become the mean of the original mean values at the two lateral sides of the profiles. The symmetrical uncertainty bounds have become the maxima of the upper bounds and the minima of the lower bounds. In the third step, additional uncertainty from the laser wavelength (±50 nm) has been introduced. This has been implemented by using a uniform variation range as λ in equation [9] on the simulation post-processing side instead of the crisp nominal value of 514.5 nm.

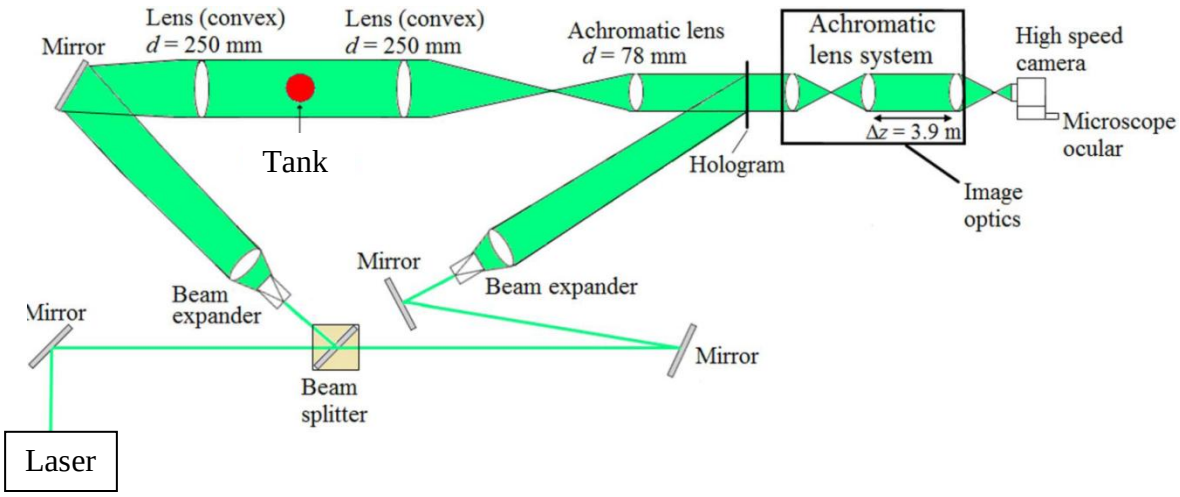

Figure 4: The experimental setup of Schönbucher et al.

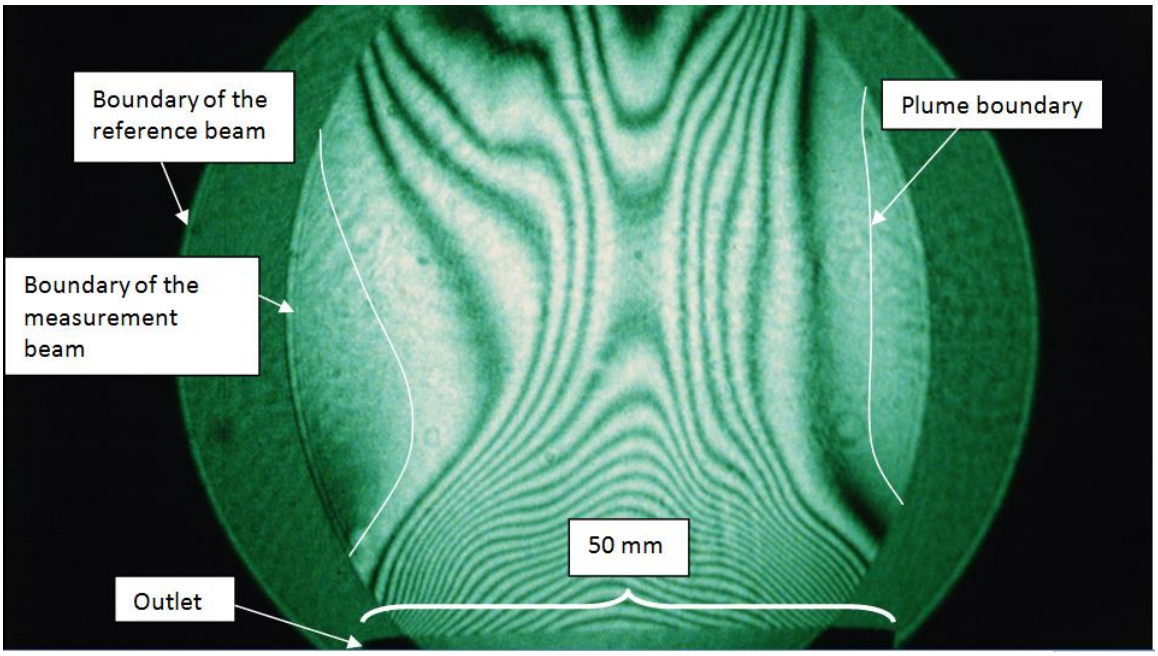

Figure 5: A typical interferometric image of the helium plume

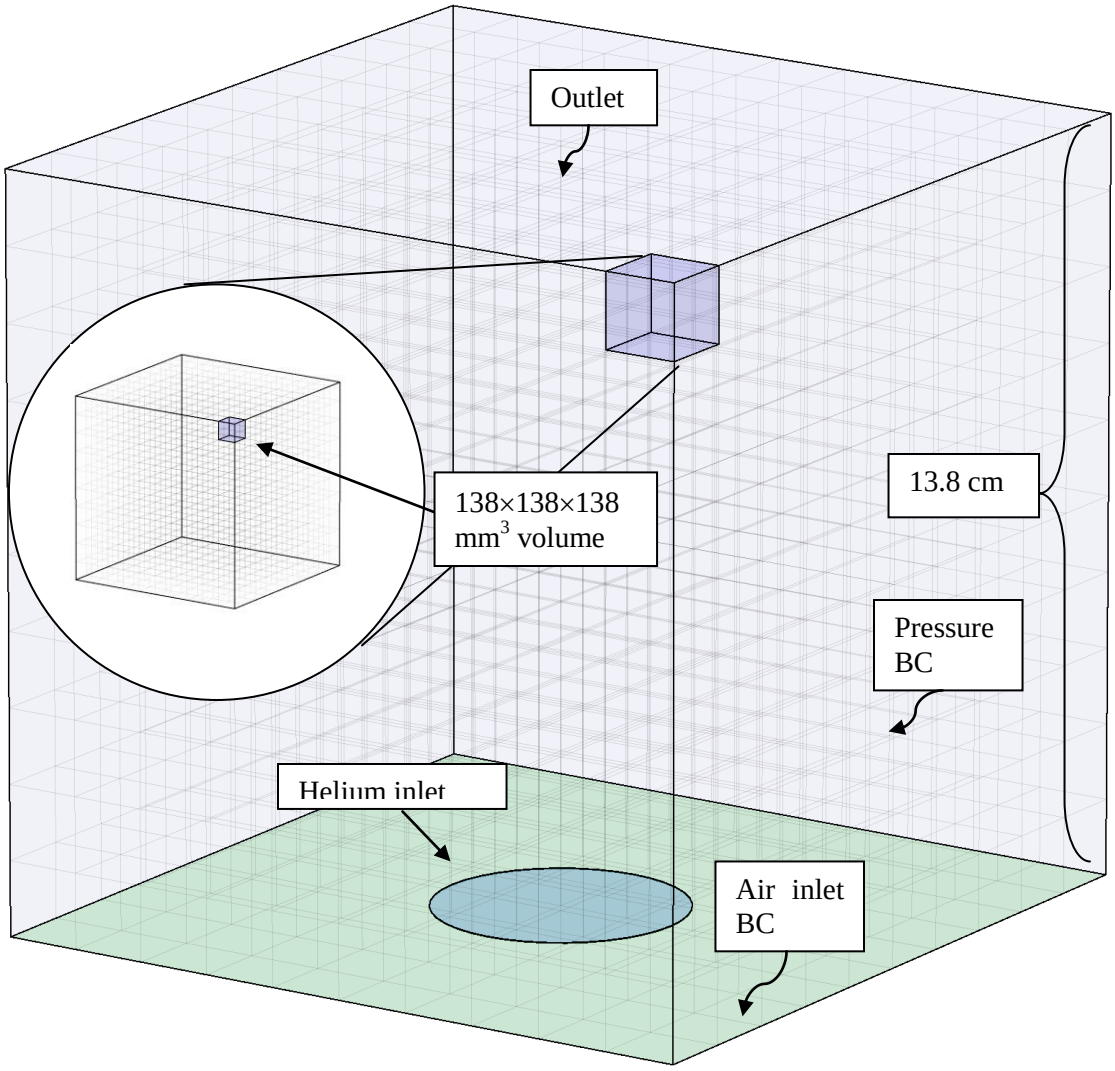

Figure 6: A schematic of the helium plume simulations.

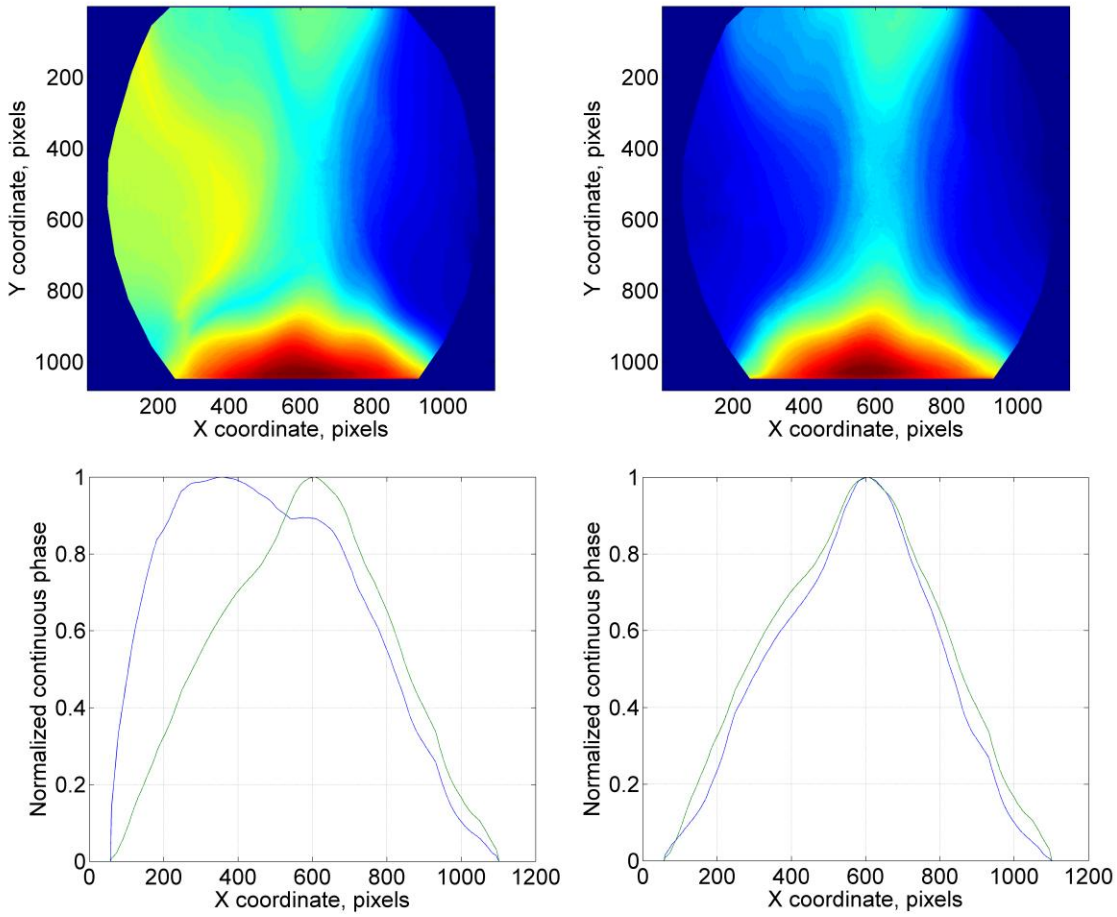

Figure 7: Unwrapping instability occurs in some cases due to the unwrapping algorithm's sensitivity to initial pixel variations. Perturbing the initial image with de-noising filters helps with this problem in most cases. Top left: badly unwrapped continuous phase map (red means high, blue means low phase values). Top right: the correct unwrapped solution to the same image. Bottom left: normalized phase profile for the incorrect phase map (blue) and the averaged correct profile superimposed (correlation strength 0.77). Bottom right: normalized phase profile for the correct phase map (blue) and the averaged correct profile superimposed (correlation strength 0.99).

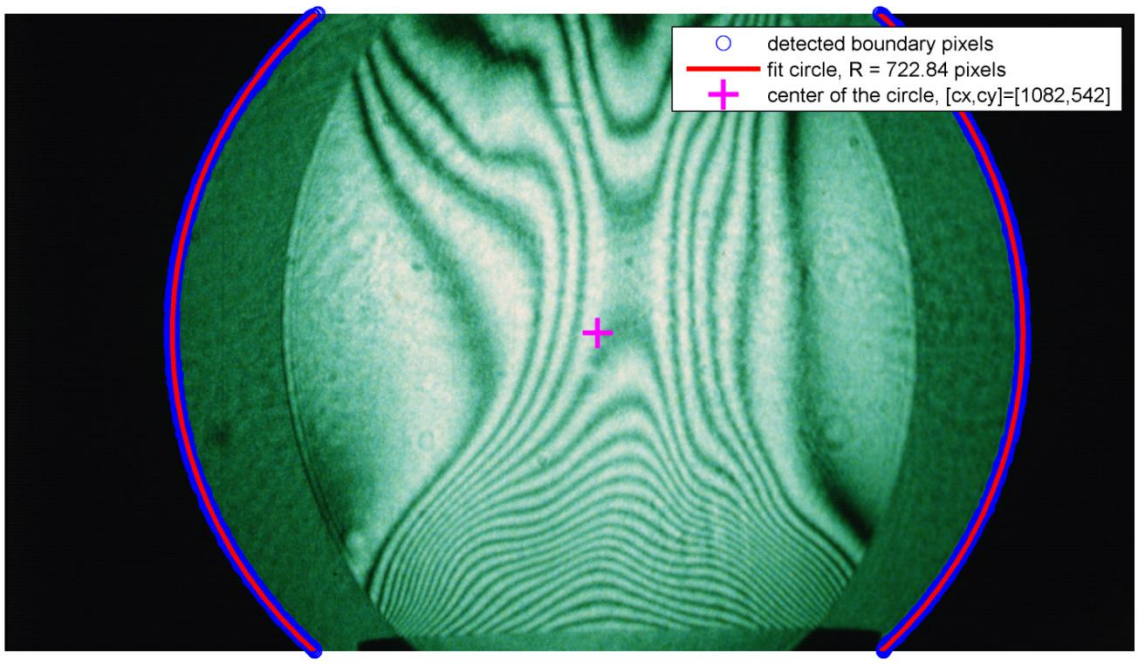

Figure 8: Automated registration procedure by detecting the spot boundaries and fitting a circle over them. Circles are fit by minimizing the sum of squared radial distances.

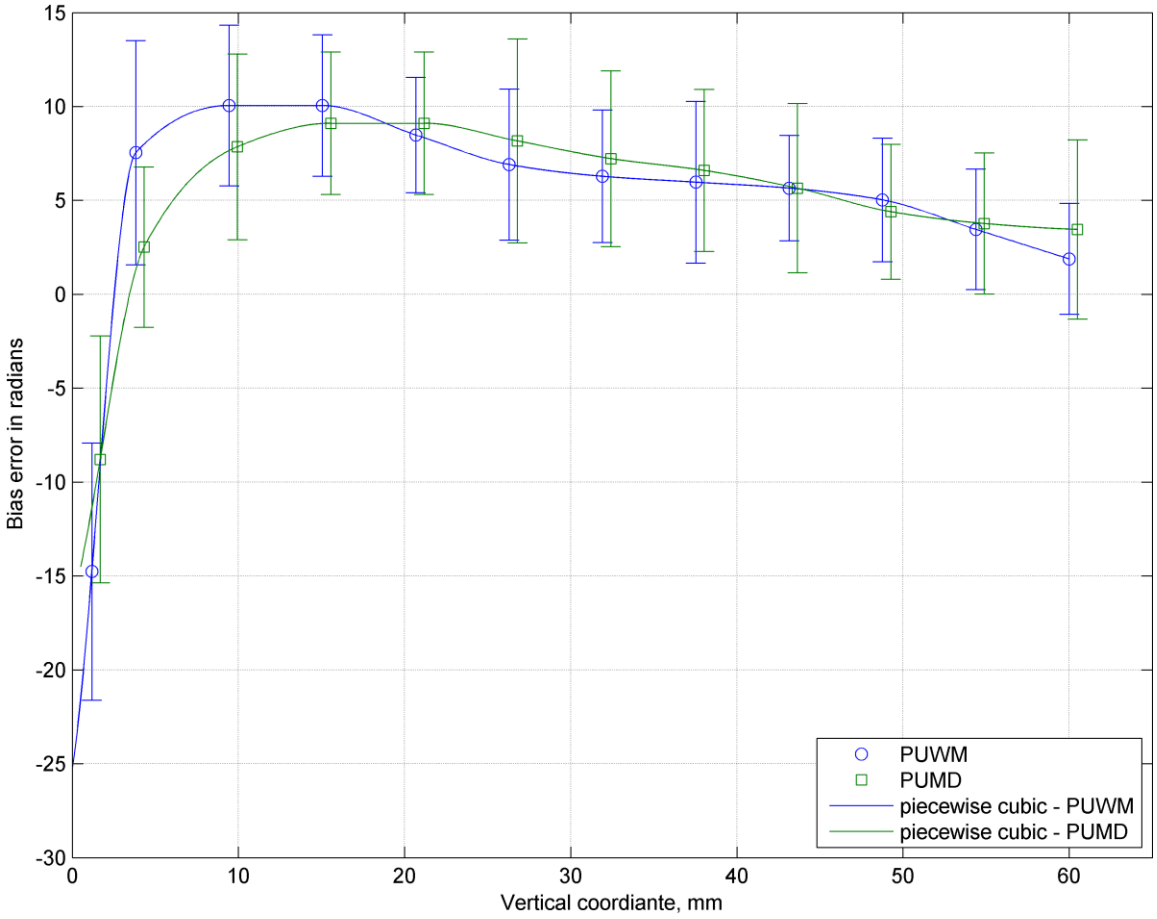

Figure 9: Averaged bias error caused by greatly varying fringe density and noise as a function of the vertical coordinate Y. These errors were the characteristic values obtained by re-calculating the fringe intensities from the phase maps obtained by the weighted multigrid (PUWM) and minimum discontinuity (PUMD) methods. The two curves are shifted slightly to improve visibility.

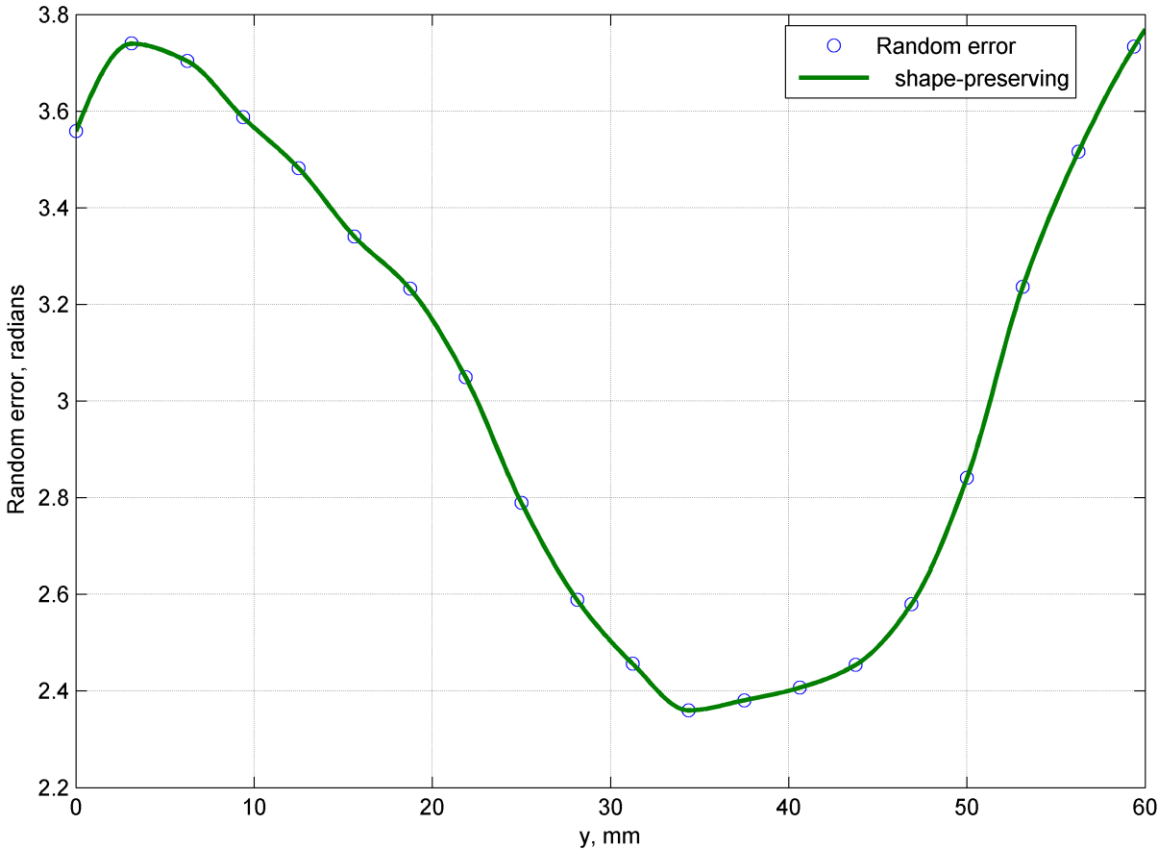

Figure 10: Averaged random error as a function of the vertical coordinate Y. These errors were the characteristic values obtained by re-calculating the intensities from the phase maps obtained by the weighted multigrid method.

CHAPTER 3

RESULTS AND DISCUSSION

In this section an overview of the most interesting results are given. This section is divided into six parts. First, general results are shown demonstrating the outputs of the methodologies. A comparison of experimental and simulation phase profile data is presented in section 3.2. Interesting results in consistency and consistency plots are shown in section 3.3. Finally, a comparison and evaluation of the performances of the two unwrapping algorithms is presented in section 3.4.

3.1 Demonstration of General Results

Figure 11 illustrates the steps of the fringe analysis procedure in a general way. The first column shows the registered and cropped fringe images. Apart from registration and cropping, the images have been converted to grayscale. The second column shows the output of the isotropic quadrature transform demodulation algorithm (discussed in section 2.3.2). The plots show the wrapped phase maps, thus the colormaps indicate values between $-\pi$ and $+\pi$. Notice that a binary mask has been applied to the cropped images in order to exclude regions from the computations that did not contain any fringes. The third column shows the unwrapped phase maps as processed by PUWM. The fourth column

shows unwrapped phase maps as processed by PUMD. As a result of the re-scaling routine (described in section 2.3.5), the continuous phase values are very close to zero near the mask boundaries. This is an example of ‘added physical insight’ to the unwrapping problem as discussed in section 1.3.3. The continuous phase gradually increases from both sides until the centerline of the plume. This is physically meaningful, as the plume is assumed to be approximately axially symmetric. As another example of introduced physical insight, this constraint has been forced on the solutions in the post-processing step as discussed in section 2.3.5. The bubbly motion of evolving instabilities in the plumes is illustrated very expressively by the sequences of continuous phase maps. The last two columns aim to visually demonstrate the slight differences between the results of the two unwrapping algorithms. These differences are described in further detail in section 3.4.

Figure 12 shows continuous phase profiles plotted versus time. The measurements were time-resolved, since the fringe images had been recorded with a high-speed camera. The frame rate was 1000 frames per second, therefore the time elapsed between two exposures was 1 millisecond. The first row shows horizontal profiles at heights 15 mm, 30 mm and 45 mm above the outlet. These profiles are two-dimensional projections of radial profiles in the three-dimensional plume. Note that among the horizontal profiles, only the profiles in the 20 mm – 40 mm height zone contain phase values close to zero. The reason of this is that the bottom and top region of the fringe patterns were not covered by the overlapping area of the two laser beams. Notice that the phase profiles are somewhat noisy. This ‘noise’ is the random error of the phase demodulation and unwrapping procedures identified as aleatory uncertainty in section 2.4.1. The second

row shows vertical phase profiles plotted versus time. From the noisiness of the vertical profiles at the centerline of the plume it is easy to see the trend in the aleatory uncertainty – higher at the bottom and top regions and lower in the middle. The vertical profiles also indicate plume dilution, expansion and instability effects as functions of height and time.

Figure 13 shows time-averaged continuous phase maps. The time-averaged maps have been used as points of comparison with simulation data. Since the image sequences contain many puff cycles that show reasonable consistency in time (no unexplainable variations within one experiment), time-averaging has been carried out by the following formula:

$$\langle \Psi \rangle_{x,y} = \frac{\sum_{n=1}^{n_f} \Psi_{x,y,n}}{n_f}, \qquad [30]$$

where $<\Psi>$ is the time-average phase map (two-dimensional), $<\Psi>_{x,y}$ is the x,y point of the time-averaged continuous phase map, n is the index of actual frame, n_f is the number of total frames and $\Psi_{x,y,n}$ is the point x,y in the continuous phase map Ψ of the n^{th} frame. As can be seen from the time-averaged phase maps, none of the four cases produced a completely axy-symmetric plume. All the plume tende to lean to the right. No significant correlation can be seen between the time-averaged continuous phase maps and helium flow rate. Time-averaged phase plots for phase maps unwrapped by both PUWM and PUMD are shown. The differences in these are further explained in section 3.4.

Figure 14 shows the computed standard deviation maps. Standard deviation maps are two-dimensional matrices, where each entry *x*,*y* is the standard deviation of the one-dimensional time series consisting of the instantaneous values of the phase sequence at coordinate *x*,*y*. Again, because the sequences contained many puff cycles, the standard deviations can be calculated by the following formula:

$$\mathrm{SD}(\Psi)_{x,y} = \frac{\sum_{n=1}^{n_f}\left(\Psi_{x,y,n} - \langle\Psi\rangle_{x,y}\right)^2}{n_f}, \qquad [31]$$

where SD(…) is the standard deviation. Standard deviation maps show the local variation in the continuous phase – the higher the value at a point, the more varied is the phase at that particular location. One expects that the standard deviation will be the lowest very close to the helium outlet, as the concentration at that location is nearly constant. The plots confirm this, although there is some variation in the first case. As in the case of time-averaged phase maps, the standard deviation maps also indicate slightly asymmetric plumes. As for correlation with flow rate, the first and fourth sets are reasonably similar in terms of flow structure, which is reasonable, since these cases had been carried out with very similar flow rates (2.25 and $2.3\cdot10^{-4}$ m^3/s). The highest variation have been observed in the case with the highest flow rate ($2.5\cdot10^{-4}$ m^3/s). In all cases, the most varying regions were close to the plume boundary. Standard deviation plots for phase maps unwrapped by both PUWM and PUMD are shown. The differences in these are further explained in section 3.4.

Figure 15 shows one-dimensional time series in the full time range of the experiments in different locations of the plume. Puff cycle frequencies, delays and overall time-consistency (stationary behavior in one experiment) are easy to obtain from these graphs. The time series in the centerline of the plume are the most consistent in time, as the amplitude of periodic phase oscillations does not change much in on experimental run. The left side of the plume (X = -16.1 mm) is more consistent than the right side (X = 16.1 mm), as the sharp jumps in phase occur more frequently in the right side. These jumps indicate badly unwrapped phase maps. These frames have been removed when computing time-averaged or standard deviation maps. Periodicity is hardly identifiable in the right side, which indicates asymmetry. For visualization purposes, only data from the first experimental case is shown here. A complete list of numerical results derived from these temporal profiles can be seen in Table 1.

Power spectra of the temporal profiles shown in Figure 15 are shown in Figure 16. Power spectra are the magnitudes of Fourier transformed time series visualizing the contributions of different frequencies in the temporal signals. Due to the nature of Fourier transformation, in power spectra, the frequency corresponding to 0 Hz is always the highest contributor (this is the so called zero-peak). For the sake of clarity, zero-peaks have been removed from these graphs. The highest contributor after the zero-peak can be identified as the puffing frequency. In all cases, the puffing frequency has been found to be between 7 and 8 Hz. The strength of periodicity can be quantified by the signal to noise ratio (SNR) of the peak corresponding to the puffing frequency in the power spectra. The signal to noise ratio is defined as:

$$\mathrm{SNR} = \frac{\mathrm{P_{max}}}{\langle \mathrm{P} \rangle}, \qquad [32]$$

where P_{max} is the power corresponding to the highest peak (zero-peak removed) and $<P>$ is the mean power of the spectrum. Values for SNR can be found in Table 1.

It is apparent that in the first experimental case, the right side of the plume showed almost no significant periodicity. For visualization purposes, only data from the first experimental case is shown here. A complete list of numerical results derived from these power spectra can be seen in Table 1.

Another quantity of interest can be the time lag between the phase in certain points of the plume. Since the continuous phase is closely periodic in time, cross correlation analysis can be applied to the time series in order to extract the average time lag between points in the plume. A typical cross correlation spectrum is shown in Figure 17. The value of the time lag indicates how much the periodic phase-time function is lagging between two in the plume. Physically, it is correlated to the velocities in the plume. Since the most dominant velocity component in the plume is the vertical one, the reference points for cross correlation have been chosen as Y = 15 mm, as the first point where the oscillations could be detected.

Table 1 summarizes the results from spectral analysis of the phase maps. Note that the puffing frequency can only be determined as accurately as the temporal resolution of the data allows. In this case, cases 1, 3 and 4 allowed for an accuracy of ±0.14 Hz and case 2 allowed for an accuracy of ±0.7 Hz. The time lag of the Y = 15 mm are obviously zero, since these points are the references of themselves. The temporal resolution of case 2 were five time lower than the rest of cases, because only every fifth frame were

available. Note that the signal to noise ratios must be interpreted by taking the lower temporal resolution into account (i.e. the lower the resolution, the lower SNR will be, since the powers will be lower). As a rule of thumb, a temporal signal with a SNR value of 150 in cases 1, 3 and 4 and a SNR value of 30 can be considered as describing a periodical signal. If the values are lower than this, the signal is too noisy or the flow is not truly periodic in that given point. Time lag values must be observed with this in mind (i.e. time lag is only meaningful when the SNR is sufficiently high).

The temporal phase signals in the left side and centerline of the plumes have been proven to be truly periodic; however the same is not true for the right side. This can be explained by the asymmetrical nature of the plumes. On average, time lag values on the left side are longer than in the centerline, indicating slower vertical velocities near the plume boundaries. Since the plume is expanding and the horizontal velocity components increase near the boundary, this is understandable. Table 1 contains only results from phase maps unwrapped by PUWM. A similar table can be found in section 3.4, providing a point of comparison for the PUMD unwrapper.

3.2 Phase Profile Comparison

In this section, the steps we took in consistency analysis are demonstrated through plots showing horizontal experimental and simulated phase profiles along with the uncertainties of the values..

As discussed in section 2.4.2, the first level of consistency testing was to include all the epistemic and aleatory uncertainties coming from algorithm sensitivity on the experimental and input parameter variation on the simulation side.

Figures 18-20 show both experimentally measured and simulated phase profiles at three different heights with uncertainties determined in this way. The data is reasonably consistent below up to 15 mm, but above that consistency diminishes. The asymmetrical behavior of the real plume caused the data to be very inconsistent at higher locations.

To remedy this issue, the assumption of axisymmetric experiments have been made and additional experimental uncertainty introduced as discussed in section 2.4.2. Figures 21-23 show the profiles resulting from this level of assumptions. Consistency improved, but in higher locations, especially near the plume boundary there were still inconsistent regions. In the third step, additional uncertainty has been introduced on the simulation side in the form of laser wavelength, as discussed in section 2.4.2.

Figures 24-26 show phase profiles resulting from the third level of assumptions on uncertainty. Again, consistency improved, but the problematic regions from the second step persisted. At this point it has been concluded that the higher experimental phase values near the plume boundary compared to simulations indicated that the experiments had been run for a significantly longer time than the simulations (in simulated time), therefore the ambience in the room where the experiments had been carried must have become contaminated with helium. To solve inconsistency issues it has been decided that new simulations are needed. This is described in more detail in Chapter 4.

Note that in this section, experimental results only from the first experimental case are presented. Table 1 summarizes the results of consistency tests.

3.3 Pairwise Consistency

In this section pairwise consistency plots are presented for the profiles shown in section 3.2. Pairwise consistency plots show the consistency measure of each two-element dataset as discussed in section 2.4.2. The plots are color coded in a way so that red shows consistent datasets and blue shows inconsistent datasets.

Figures 27-35 show pairwise consistency plots for the phase profiles presented before. The data with the first level of uncertainty quantification showed no full pairwise consistency at all. Each height contained at least one inconsistent dataset (with a consistency measure below zero). Generally, this can suggest two things: either the simulation or the experiment were carried out in an incorrect way or the uncertainties were underestimated. Since the evolution of the phase profiles as a function of height was similar in both the simulated and experimental cases, we assumed the latter.

In the second level of uncertainty quantification, the experimental plume has been assumed to be axisymmetrical. Any deviation from axisymmetry has been assumed to be uncertainty. Introducing this additional source of uncertainty on the simulation side made the data much more consistent with simulation data. In the best case (in the case of the third experimental run), the profiles have been consistent up to heights of 32.4 mm in the plume. Higher up in the plume inconsistent regions appeared near the X = -16.1 mm and X = 16.1 mm regions. These inconsistent regions suggested helium contamination in the ambience that showed as flatter phase profiles in the experimental data. These regions

present themselves as blue bands at datasets 6 to 8 and 29 to 31 in the pairwise consistency plots.

Introducing additional uncertainty on the simulation side in the form of laser wavelength uncertainty (see section 2.4.2) did not solve this problem. The blue bands persisted after the addition of this uncertainty source. The general consistency of the data has improved, as in the best case (third experimental run), the profiles were consistent up to 35.1 mm height.

The consistencies of each experimental case have improved, but as long as the pairwise tests show no complete consistency, there is no reason to proceed to full consistency analysis. As with pairwise plots, if only one two-element dataset is inconsistent, the whole dataset will be inconsistent, therefore if as long as all the pairwise tests are not consistent on their own, the full dataset consisting all the heights will not be consistent.

Due to this characteristic of the pairwise tests, it is convenient to define an overall consistency measure for a pairwise set of two-element datasets. Such an overall measure can be defined as the lowest consistency measure value in the pairwise test. This definition is convenient, because as long as this value is negative, there will be an inconsistent two-element dataset in the pairwise test which will ultimately make the whole dataset inconsistent. This overall consistency measure is plotted versus height in Figure 36.

It is easy to see that the consistency profile never reached zero in the first level. The difference between the second and third levels is not very significant. The third experimental case has been proved to be the most consistent among the four. Note that

the lowest value of the overall consistency measure is not bounded, but the highest value is unity.

3.4 Performance Comparison of the Two Unwrappers

In this section the performance of the PUMD unwrapper is compared to the performance of PUWM. This is done in two ways. First, the results derived from spectral analysis using PUMD are shown compared to those of PUWM in Table 2. Second, a comparison of overall consistency measure values is shown in Figure 37.

Table 2 shows frequency-related properties of all four experimental cases determined from phase maps unwrapped by PUMD. The values for puffing frequency, time lag and SNR are given relative to values determined by using PUWM in the following way:

$$\mathrm{C_{PUMD}} = \mathrm{A_{PUMD}} - \mathrm{A_{PUWM}}, \qquad [33]$$

where C_{PUMD} is the comparison value, A_{PUMD} is a property derived from phase maps unwrapped by PUMD and A_{PUWM} is a property derived from phase maps unwrapped by PUWM. In this way a negative *C* value indicates a lower *A* value for PUWM. This is a convenient way to compare SNR values, as higher SNR indicate a more reliable unwrapping routine.

There are no significant differences between the two unwrappers in terms of puffing frequency time lag determination. However, there are significant differences in SNR. Overall, PUMD has been proved to be less reliable than PUWM with respect to identifying obviously present periodicities.

Figure 37 shows overall pairwise consistency measure profiles of phase data unwrapped by PUMD. Generally the consistency values were close to zero, either on the positive or negative side, which indicates only slight consistency or inconsistency. Strictly speaking, PUMD phase maps were more consistent than PUWM maps, but only due to the higher uncertainties introduced by the higher aleatory uncertainties of the PUMD unwrapper. Along with more frequent sharp jumps in temporal series (as mentioned in section 3.1) this is another sign of PUMD being less reliable and producing more stochastic oscillations in the phase data. In the best case (third experimental case), PUMD maps were consistent up to 42 mm height. The inconsistent upper regions produced half the inconsistency as the phase data unwrapped by PUWM.

Since neither PUWM nor PUMD has been able to achieve complete pairwise consistency, it has been concluded that the sources for experimental and simulation uncertainties have been exhausted. No further reasonable sources of uncertainties have been found to be worth implementing. It has been concluded that the inconsistent regions near X = -16.1 mm and X = 16.1 mm had been caused by helium contamination in the room where the experiments had been run. For this reason, additional simulations have been designed and started. These simulations have not been conclusive by the time of submittal this thesis. For future ideas to improve consistency, please refer to Chapter 4.

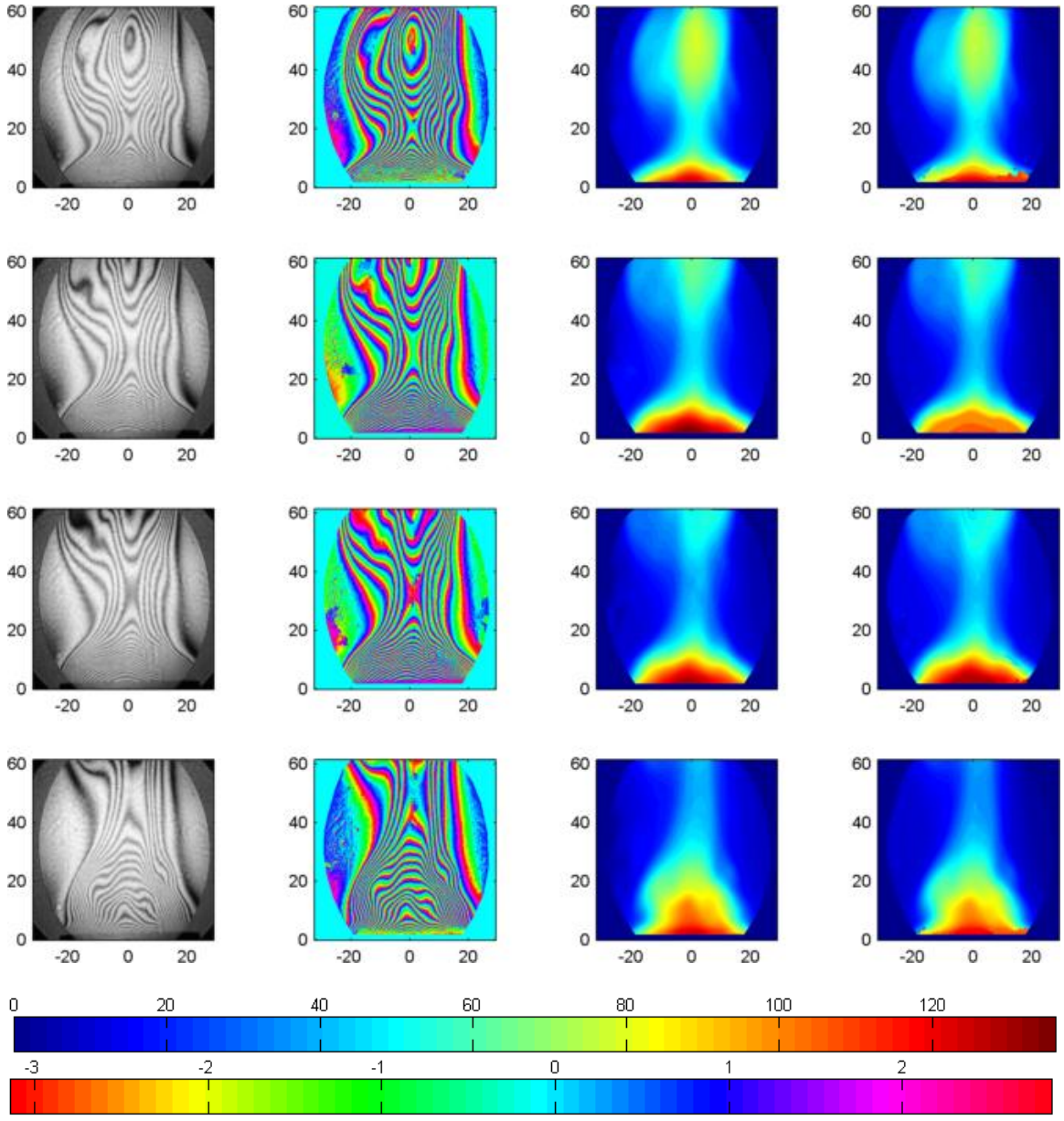

Figure 11: A demonstration of general results. Units are millimeters. The left column shows the original images converted to grayscale, registered and cropped. The second column from the left shows the demodulated modulo 2π phase maps. The third and the last columns show continuous phase maps unwrapped by PUWM and PUMD in radians, respectively. The figure shows a complete puff cycle of the helium gas in four steps.

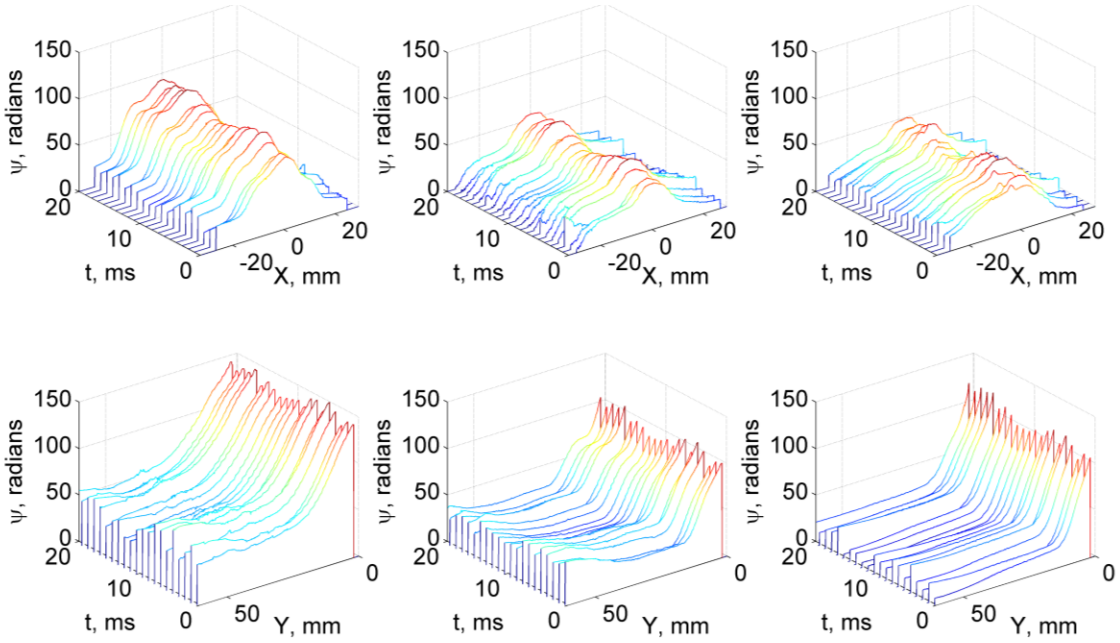

Figure 12: Time series of horizontal (top row) and vertical (bottom row) phase profiles. The continuous phase maps have been obtained by the PUWM unwrapper. The time between two frames is 1 millisecond. The oscillations are caused by the sensitivity of the algorithm to pixel variation. Top left: horizontal profiles at 15 mm high in the plume. Top center: profiles at 30 mm high in the plume. Top right: profiles at 45 mm high in the plume. Bottom left: vertical profile at X = -16.1 mm. Bottom center: Bottom right: vertical profile at the centerline of the plume. Bottom right: Bottom left: vertical profile at X = 16.1 mm.

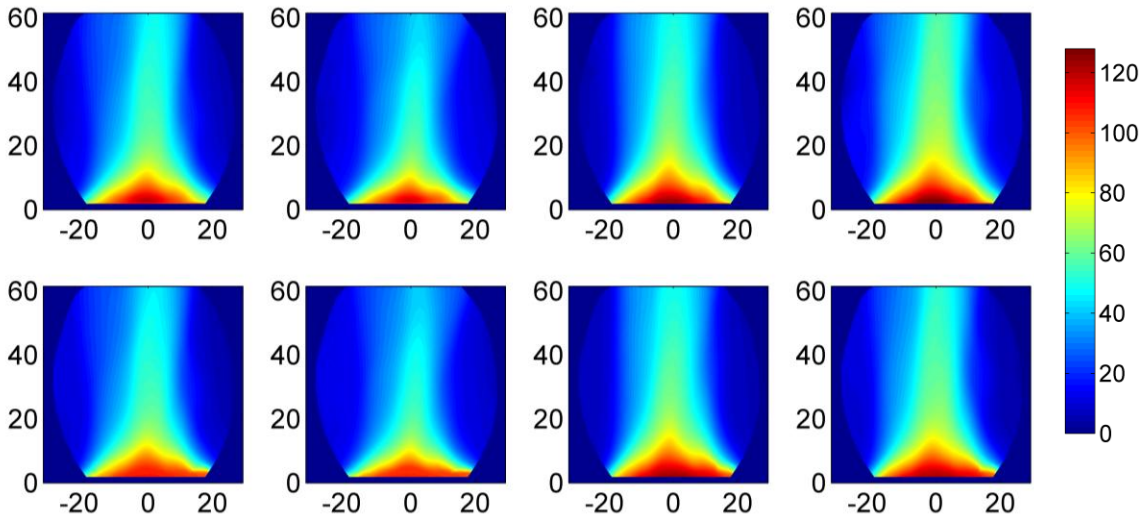

Figure 13: Time-averaged phase maps. The top row shows continuous phase maps unwrapped by PUWM. The bottom row shows phase maps unwrapped by PUMD. From the left to the right the plots show the results from the four experiments. The spatial units are millimeters, the phase is in radians.

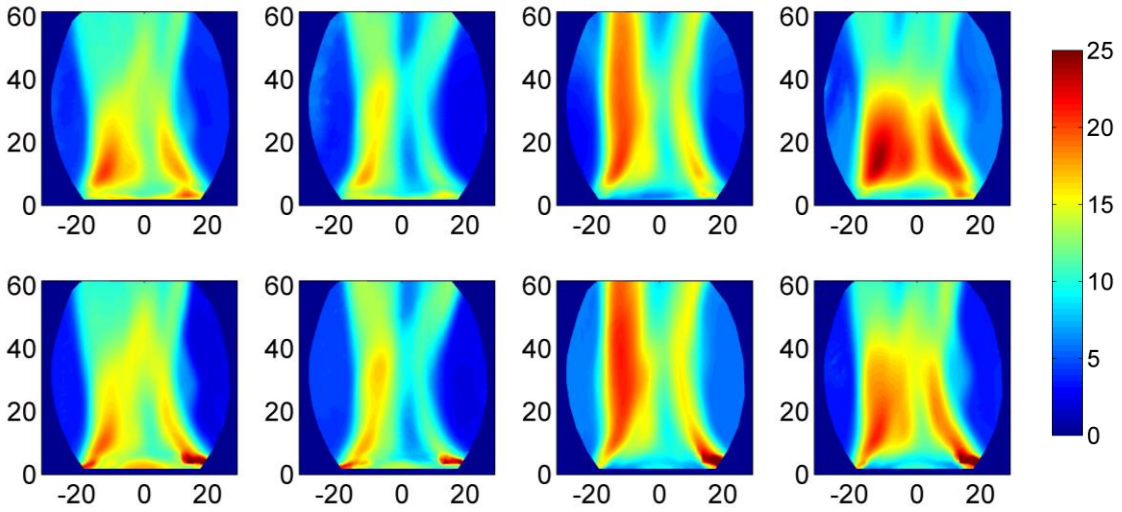

Figure 14: Standard deviations of the time series of unwrapped maps. The top row shows continuous phase maps unwrapped by PUWM. The bottom row shows phase maps unwrapped by PUMD. From the left to the right the plots show the results from the four experiments. The spatial units are millimeters, the phase is in radians.

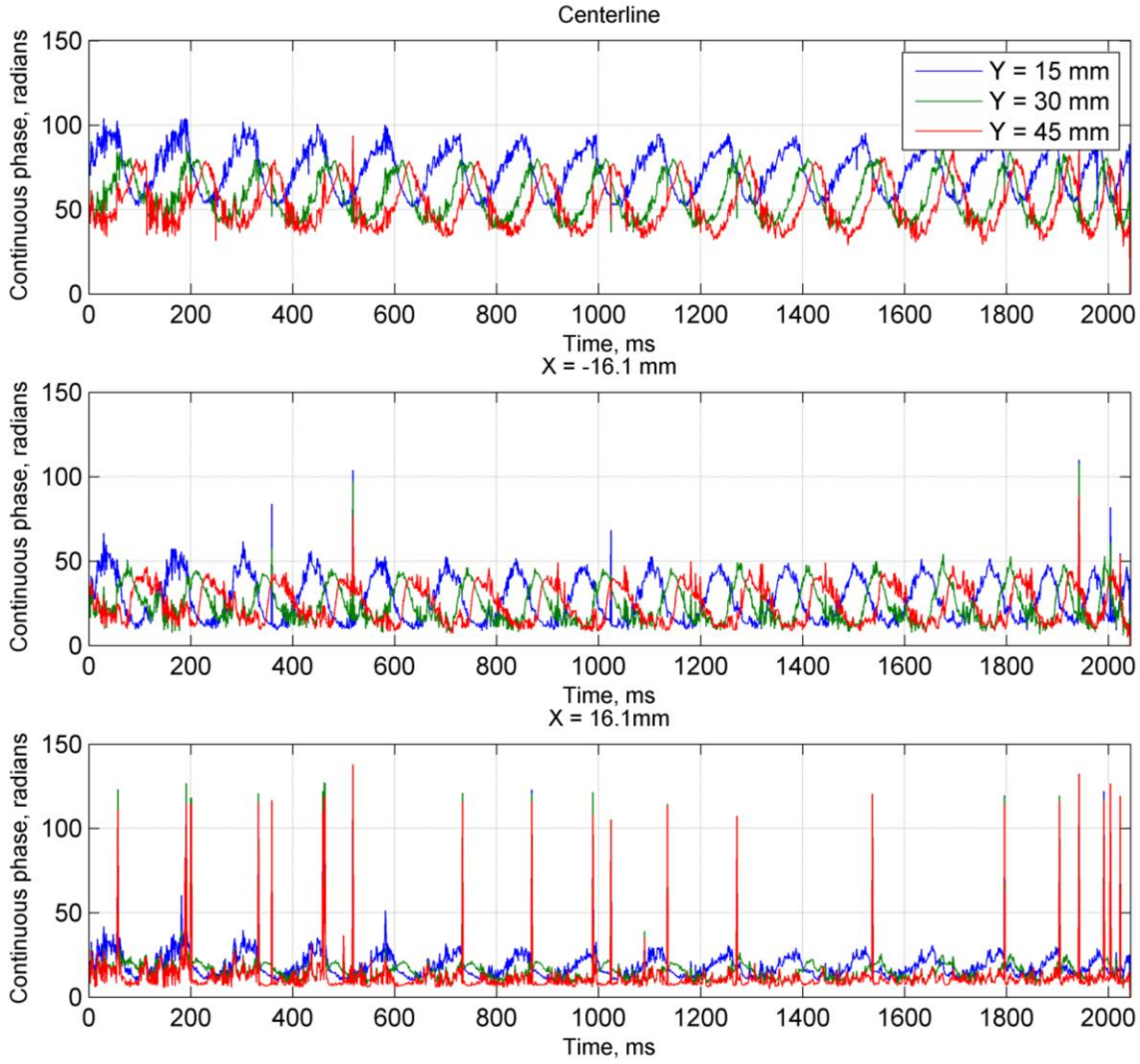

Figure 15: Temporal profiles of different locations (one-dimensional spots) in the plume. The high jumps are caused by faulty unwrapping. The reliability of the unwrapping is higher near the outlet in terms of temporal smoothness. These profiles have been generated by batch-processing continuous phase maps unwrapped by PUWM. Phase maps are from the first experimental case.

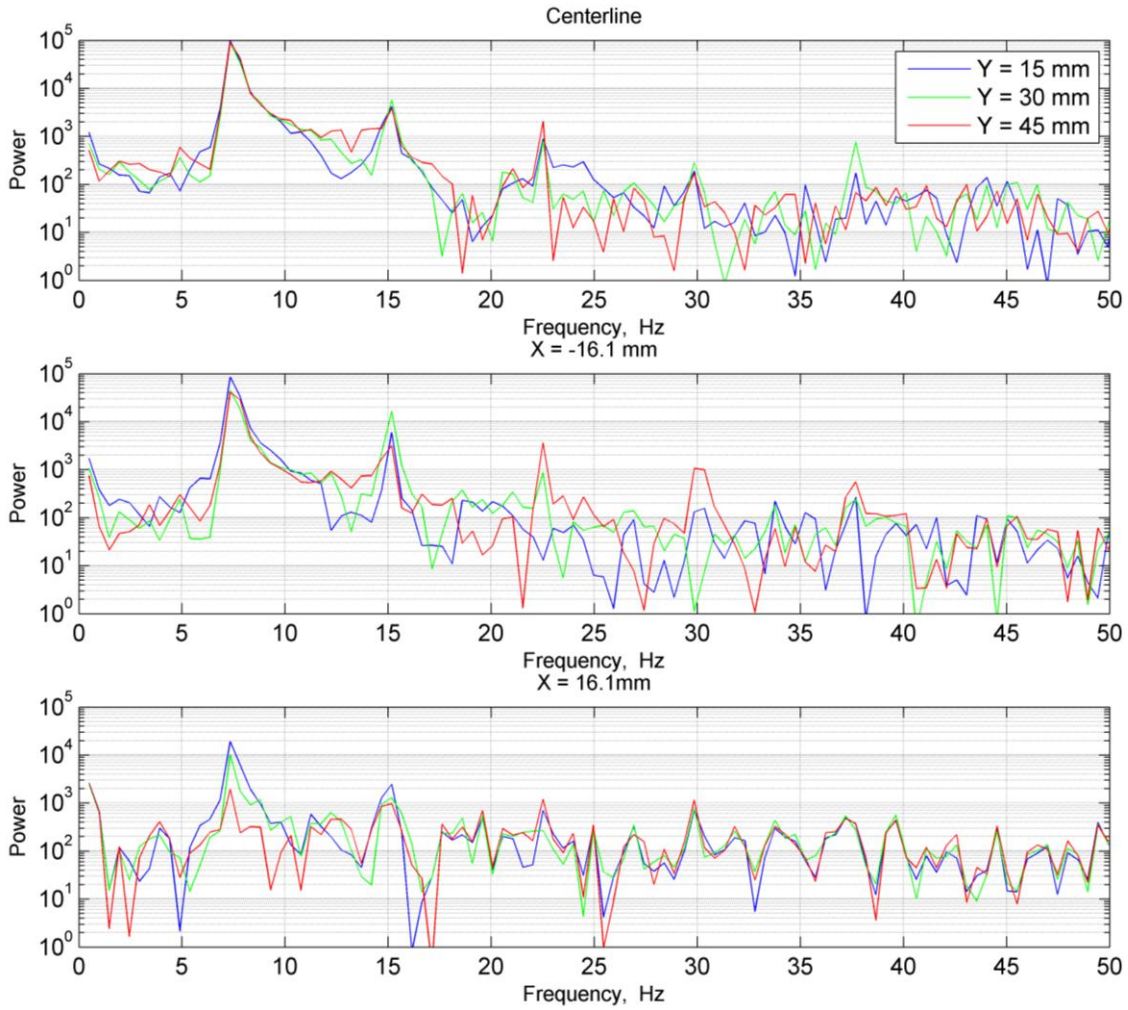

Figure 16: Power spectra of the phase of different time series of one-dimensional spots in the plume. The puffing frequency is the highest power contributor. Its value is around 7.3 Hz. This value is not affected much by spatial location. The unwrapper here was PUWM. Phase maps are from the first experimental case.

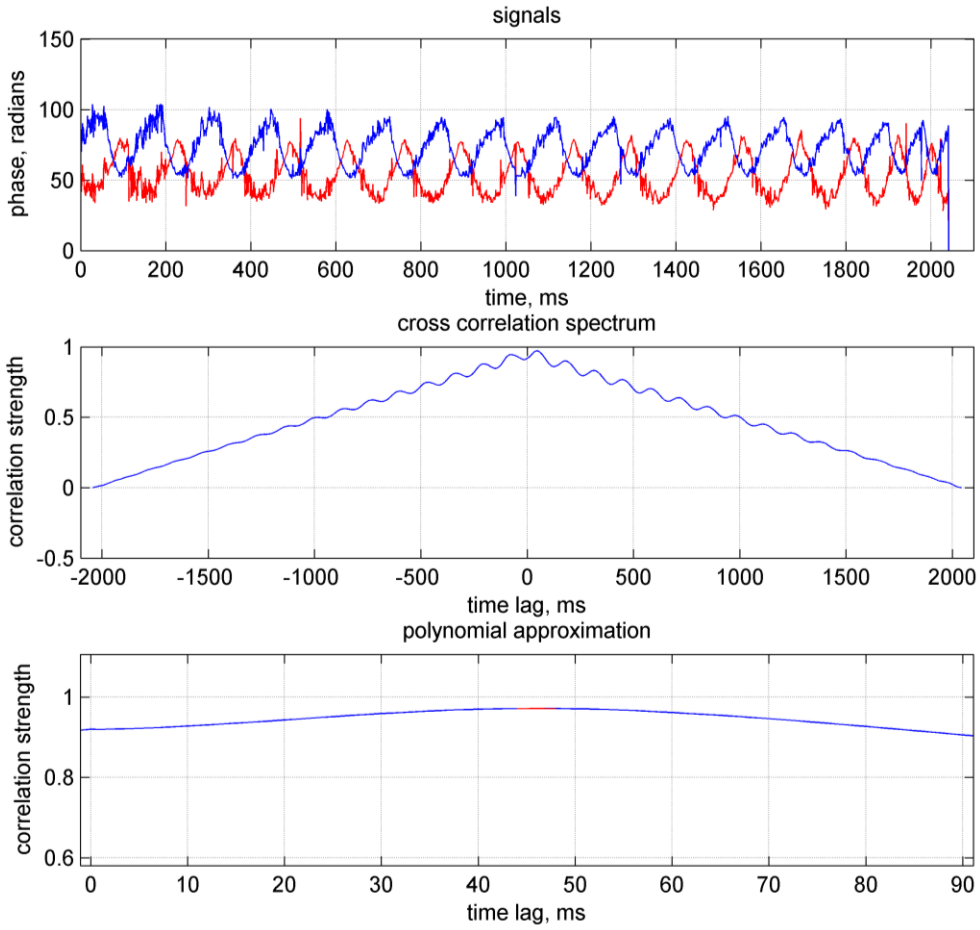

Figure 17: Cross correlation analysis of phase signals. The phase-time signals in two points are shown in the uppermost plot. The middle plot shows the cross correlation spectrum of the two signals. A polynomial curve is fit around the maximum of the spectrum in order to determine the time lag more accurately (in red, bottom plot). The time lag shown here is 46.02 ms.

Table 1: Results of spectral analysis. Phase maps have been unwrapped by PUWM.

	puffing frequency, Hz			time lag, ms			SNR		
	Y = 15 mm	Y = 30 mm	Y = 45 mm	Y = 15 mm	Y = 30 mm	Y = 45 mm	Y = 15 mm	Y = 30 mm	Y = 45 mm
case 1									
X = -16.1 mm	7.34	7.34	7.34	0	40.44	69.14	634.39	448.36	441.02
center	7.34	7.34	7.34	0	25.06	46.02	698.13	682.68	603.34
X = 16.1 mm	7.34	7.34	7.34	0	2*	1.19*	142.92	74.62	18.15
case 2									
X = -16.1 mm	7.05	7.05	7.05	0	10	60.5	58.55	18.59	53.69
center	7.05	7.05	7.05	0	10	30	96.72	147.75	123.91
X = 16.1 mm	7.05	7.05	7.05	0	10*	10*	6.41	6.08	6.89
case 3									
X = -16.1 mm	8.38	8.38	8.38	0	40.07	68.21	1609.1	1509.6	1434.8
center	8.38	8.38	8.38	0	23.01	39.26	1521.2	1577.7	1405.3
X = 16.1 mm	8.38	8.38	8.38	0	2*	2*	195.45	31.67	33.69
case 4									
X = -16.1 mm	8.02	8.02	8.02	0	36.26	55.81	1437.7	1296.3	1014.8
center	8.02	8.02	8.02	0	20.37	40.19	1328.2	1018.8	1038
X = 16.1 mm	8.02	8.02	8.02	0	2*	2*	375.03	202.36	45.12

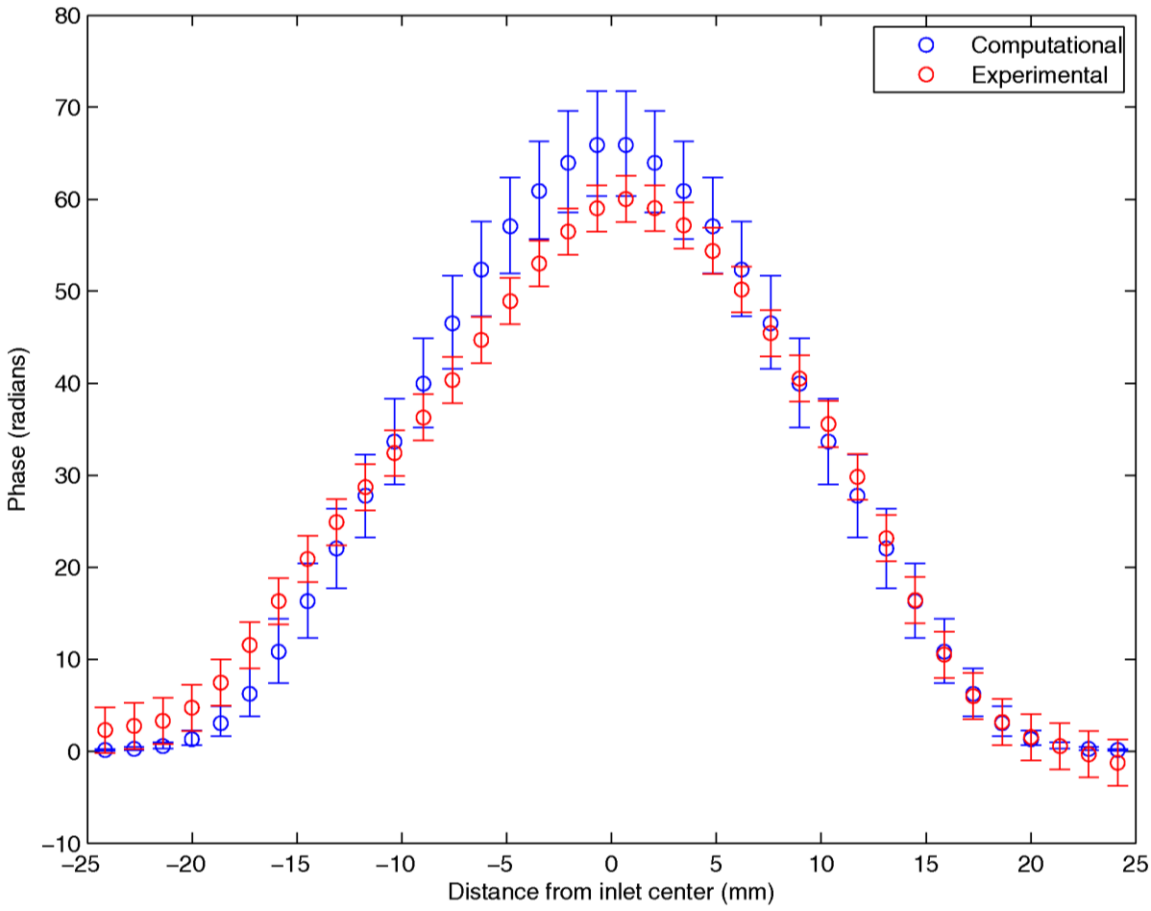

Figure 18: Phase profile comparison with the first level of assumptions on uncertainty. Height: 15 mm.

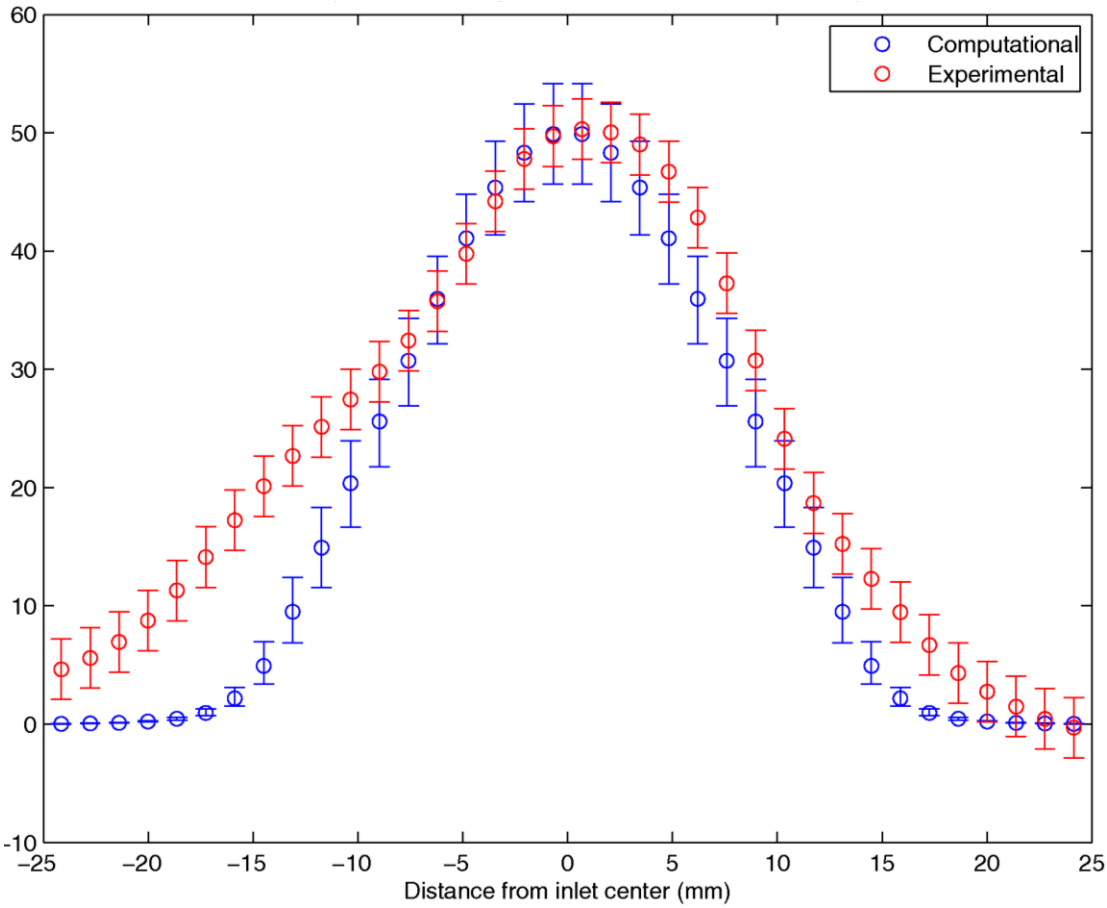

Figure 19: Phase profile comparison with the first level of assumptions on uncertainty. Height: 30 mm.

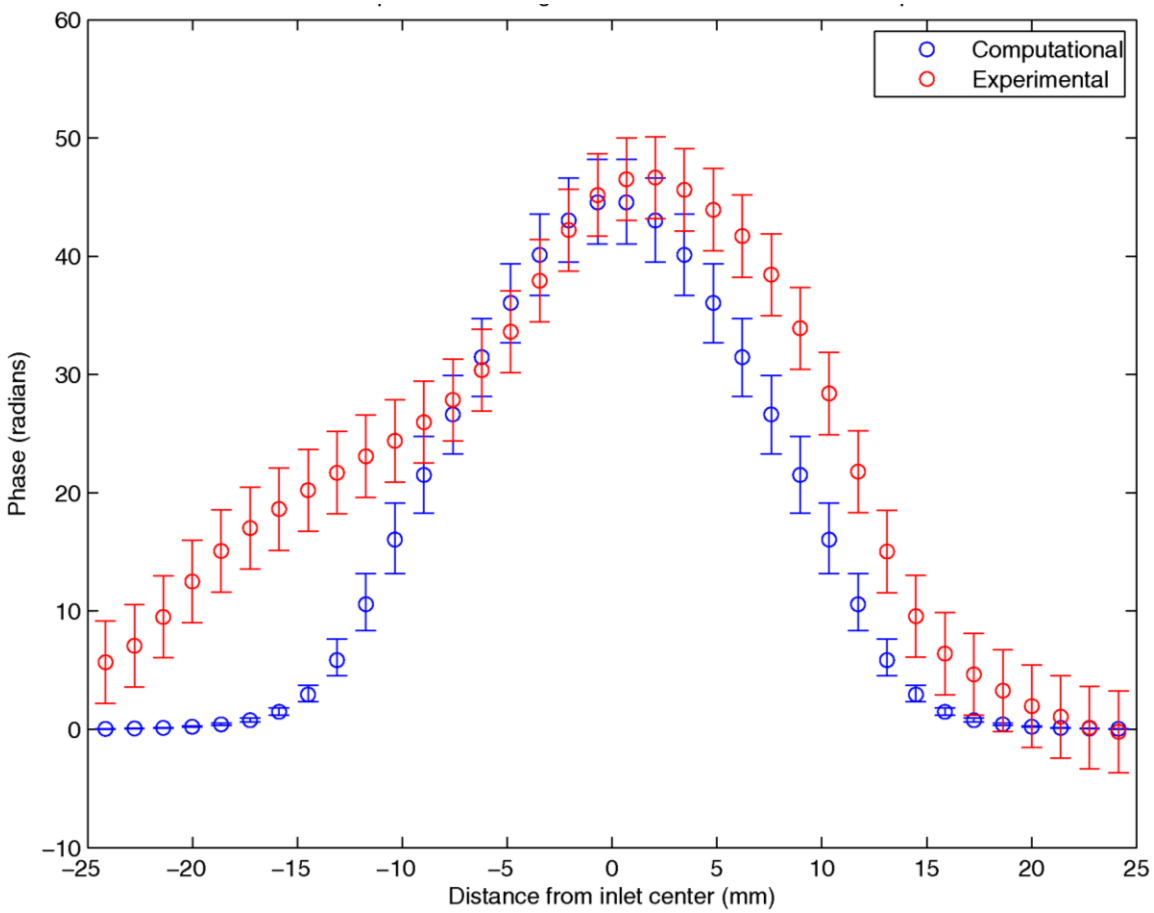

Figure 20: Phase profile comparison with the first level of assumptions on uncertainty. Height: 45 mm.

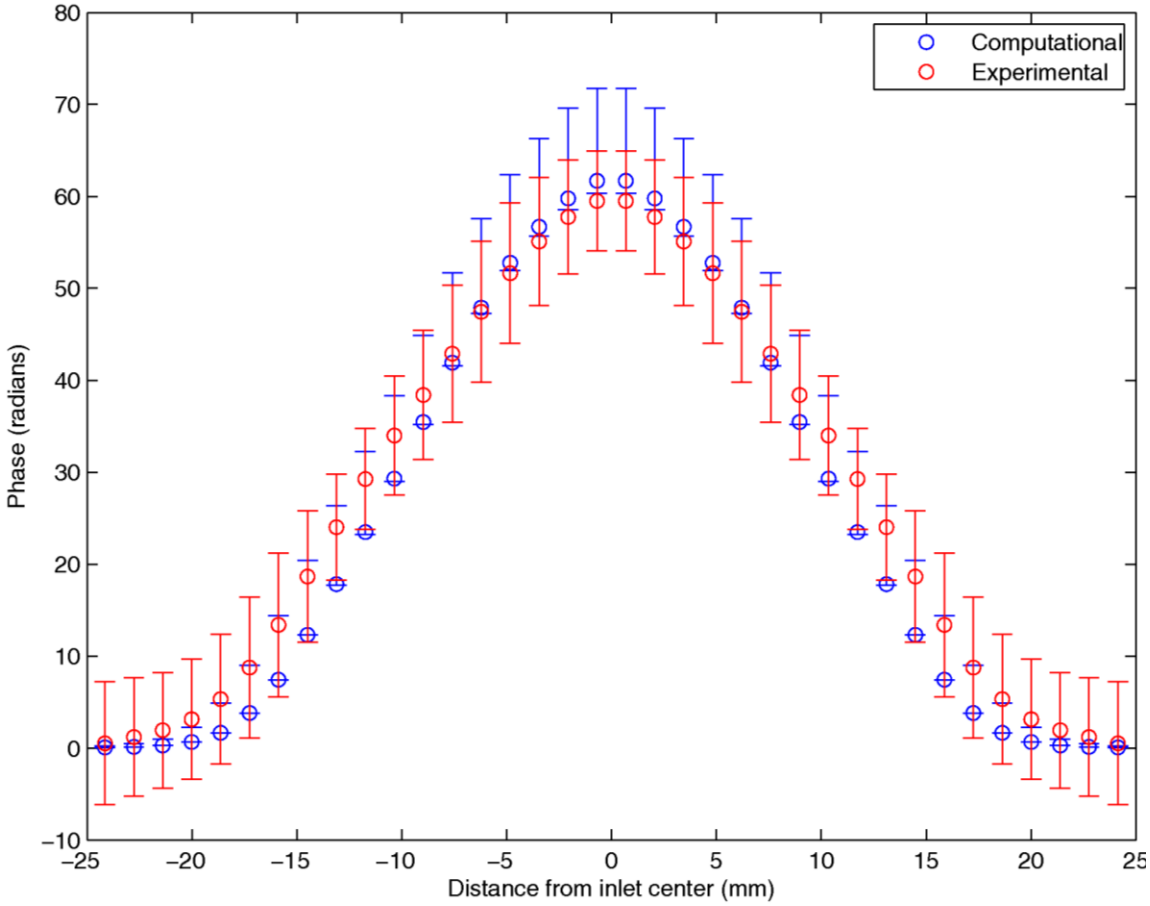

Figure 21: Phase profile comparison with the second level of assumptions on uncertainty. Height: 15 mm.

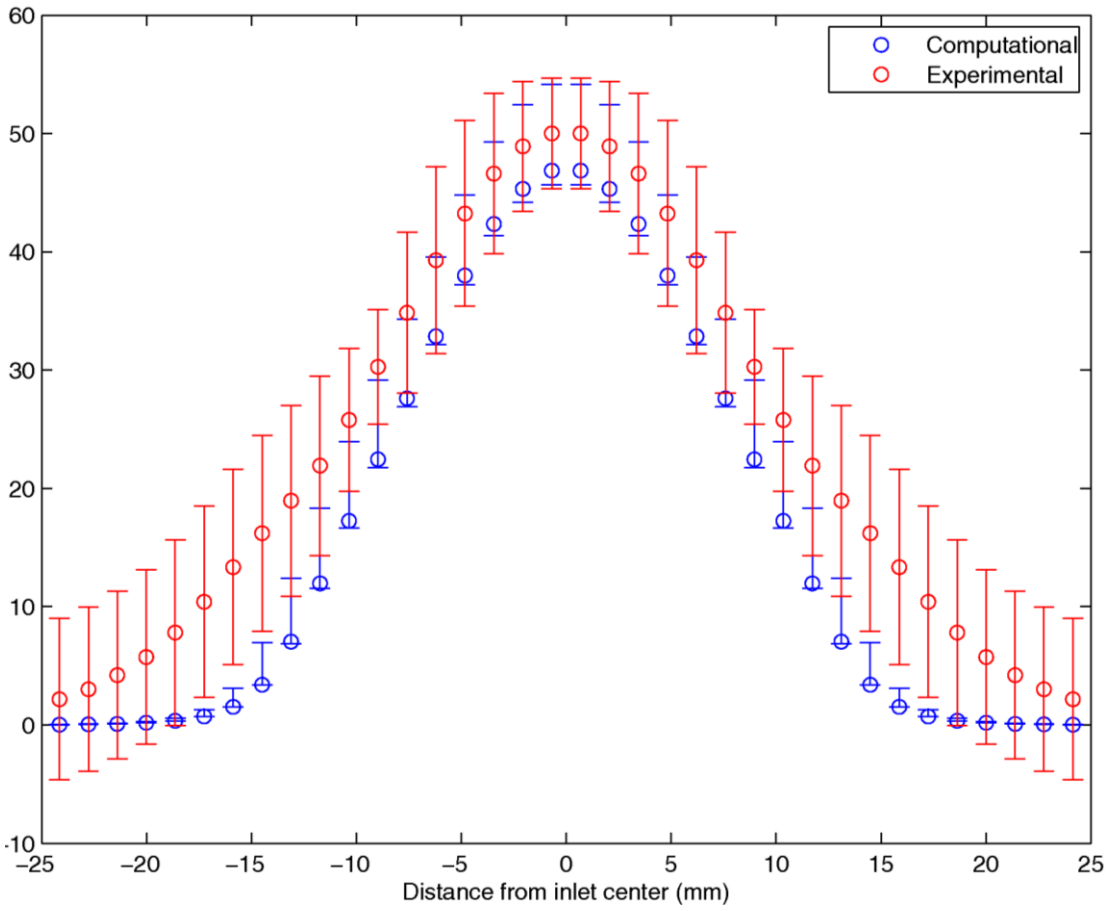

Figure 22: Phase profile comparison with the second level of assumptions on uncertainty. Height: 30 mm.

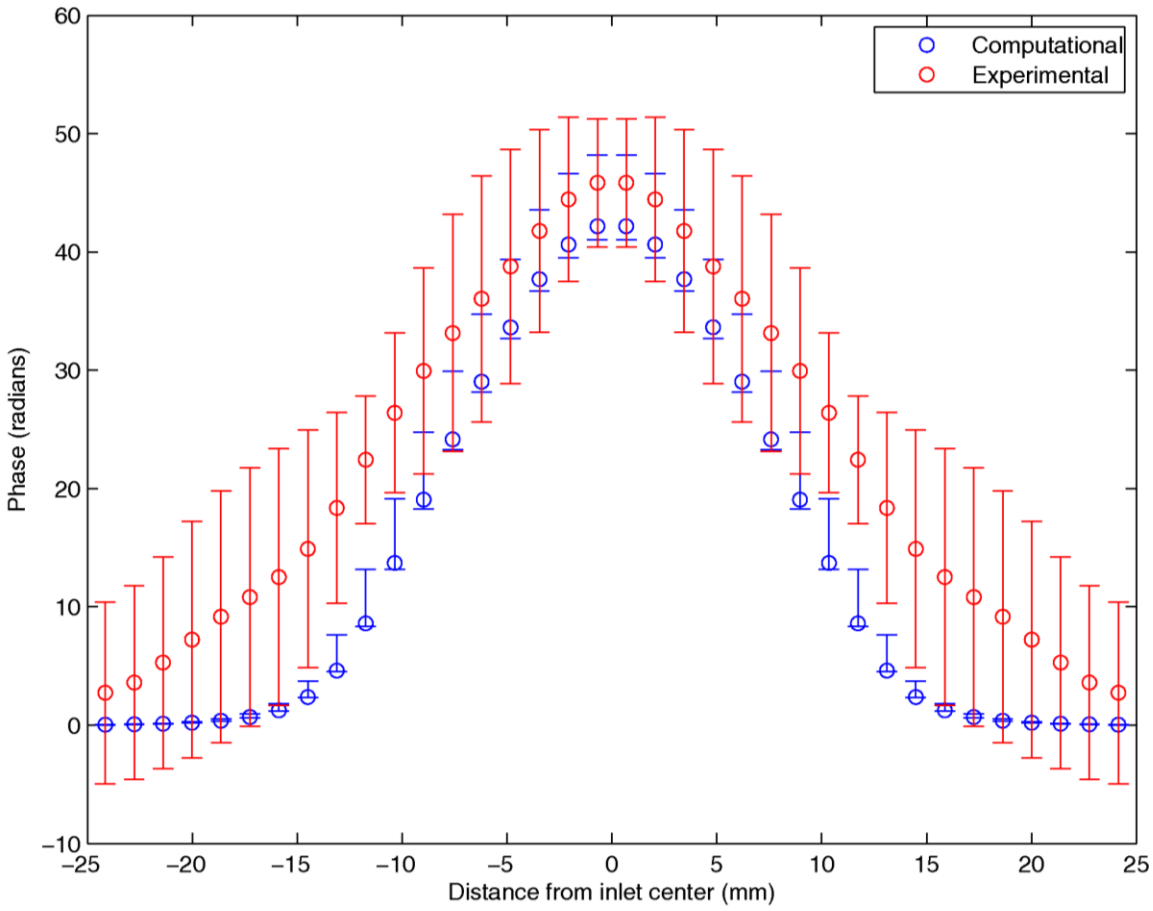

Figure 23: Phase profile comparison with the second level of assumptions on uncertainty. Height: 45 mm.

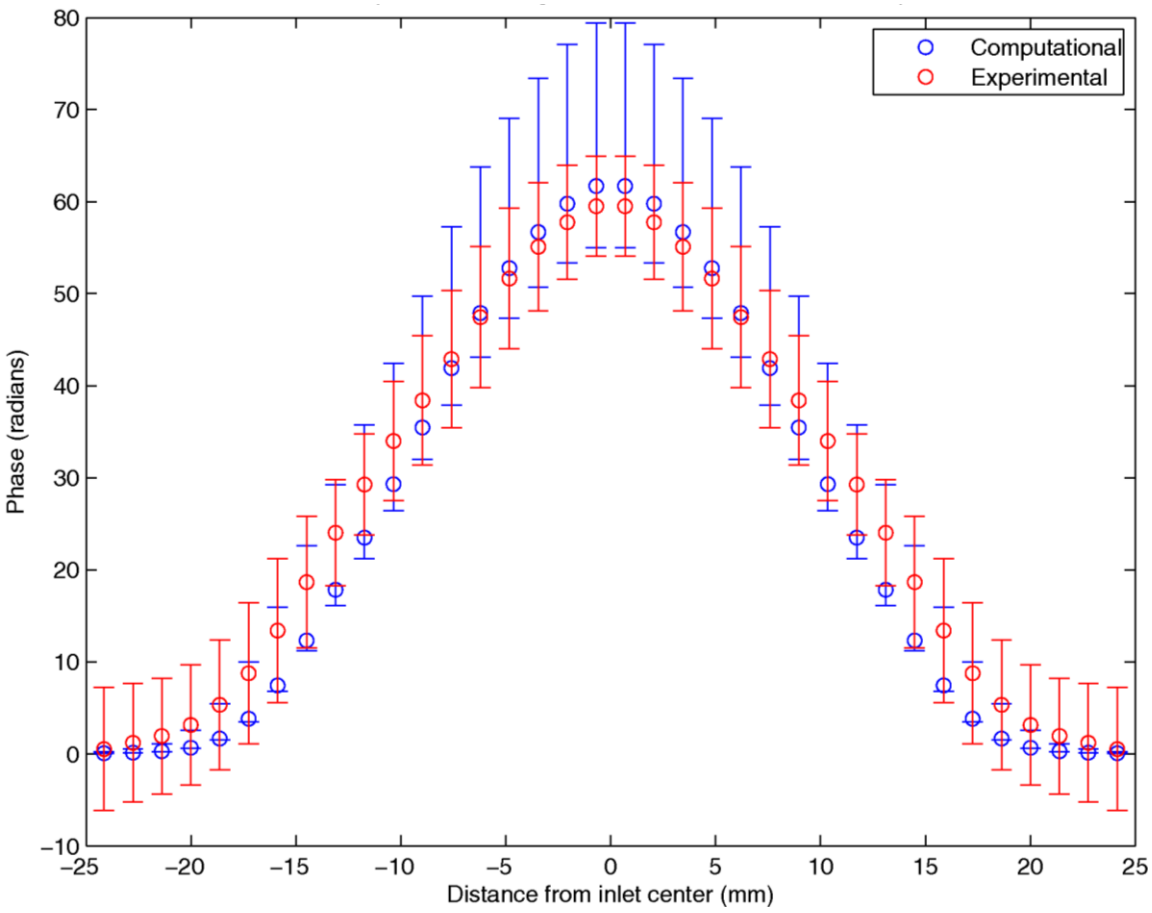

Figure 24: Phase profile comparison with the third level of assumptions on uncertainty. Height: 15 mm.

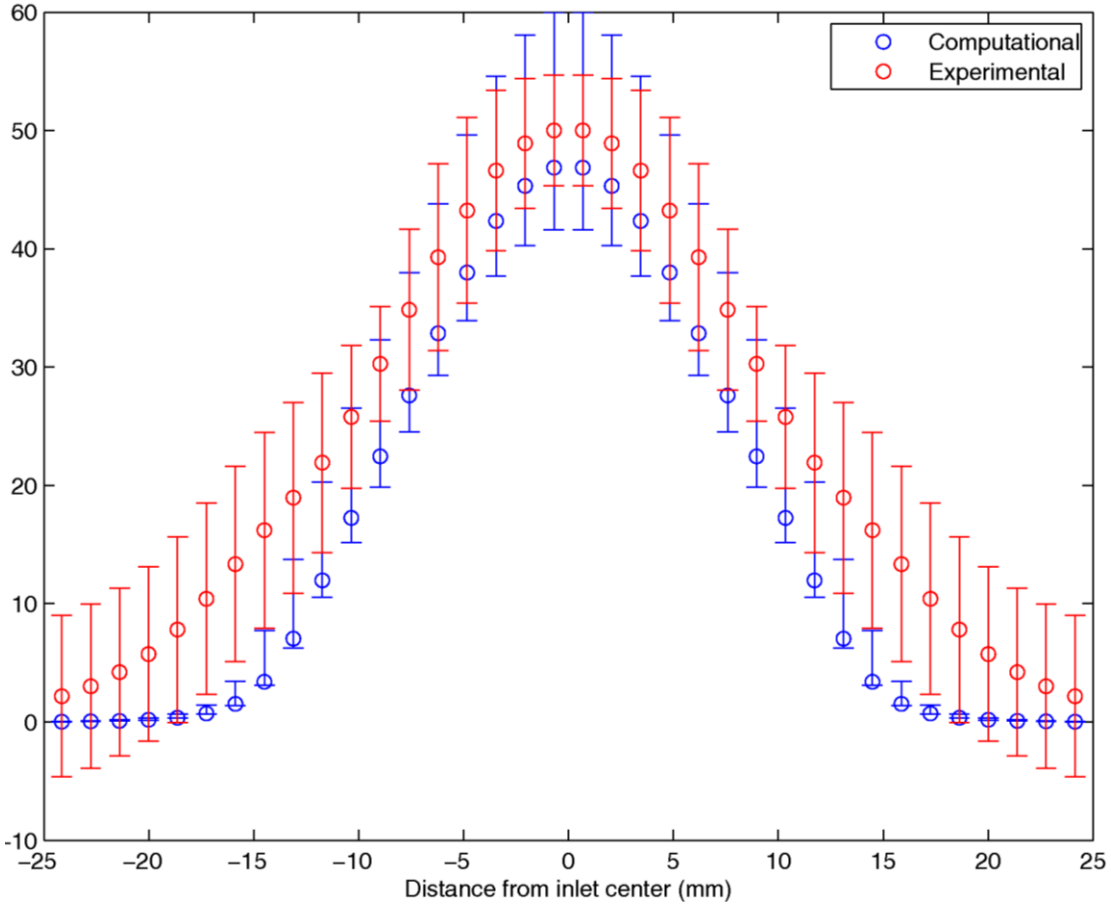

Figure 25: Phase profile comparison with the third level of assumptions on uncertainty. Height: 30 mm.

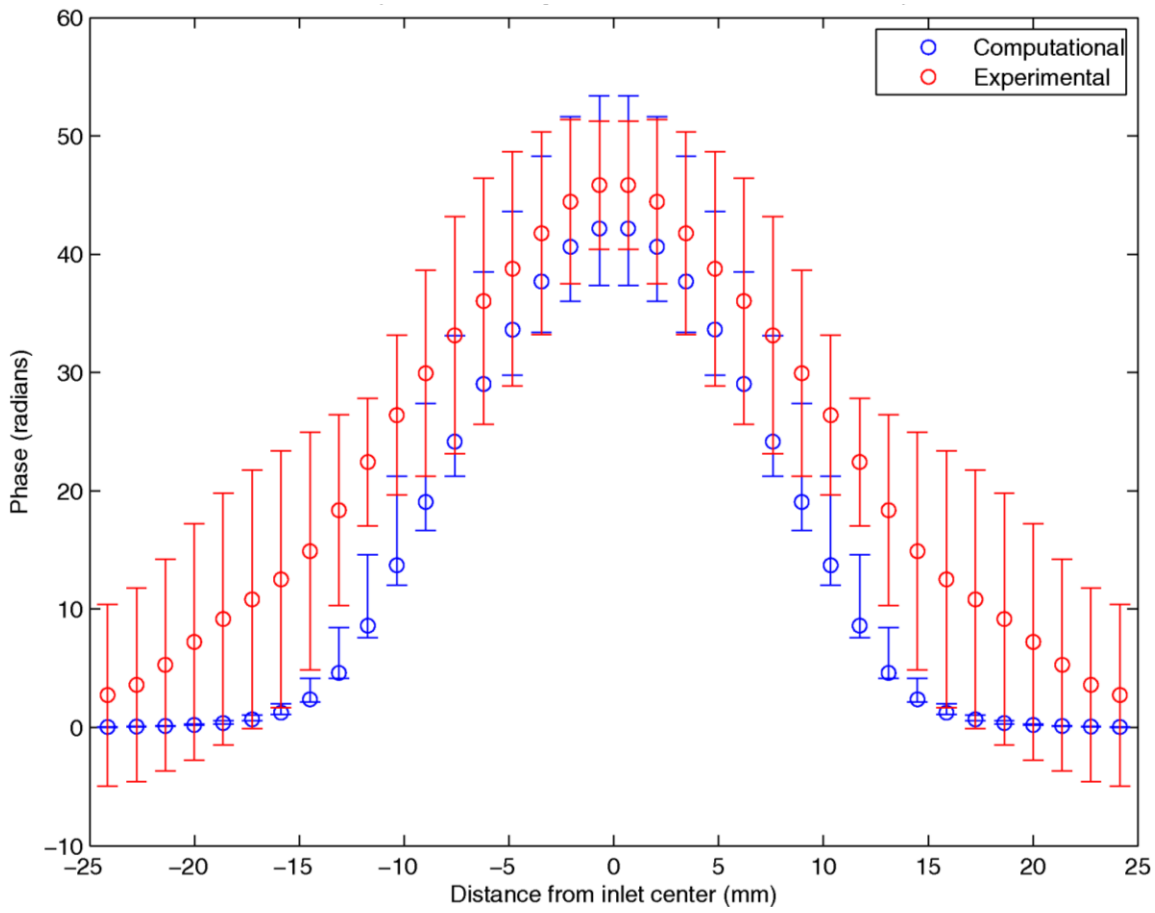

Figure 26: Phase profile comparison with the third level of assumptions on uncertainty. Height: 45 mm.

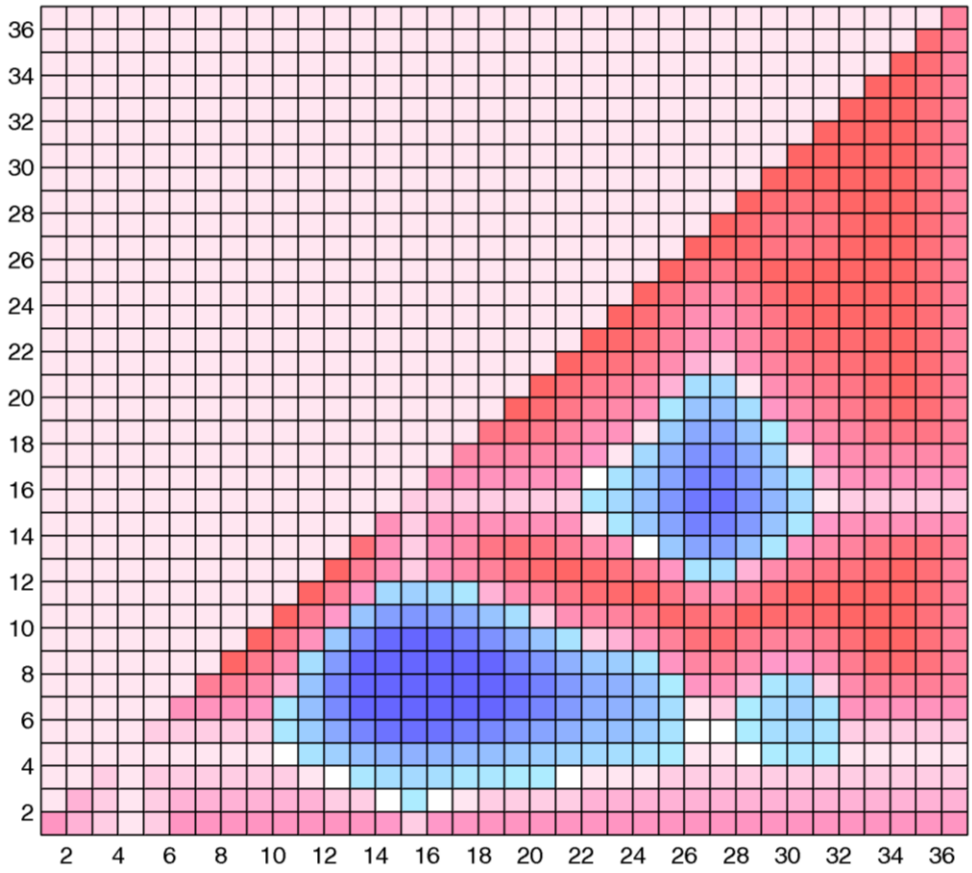

Figure 27: Pairwise consistency plots for the first level of assumptions on the uncertainty.

Height: 15 mm.

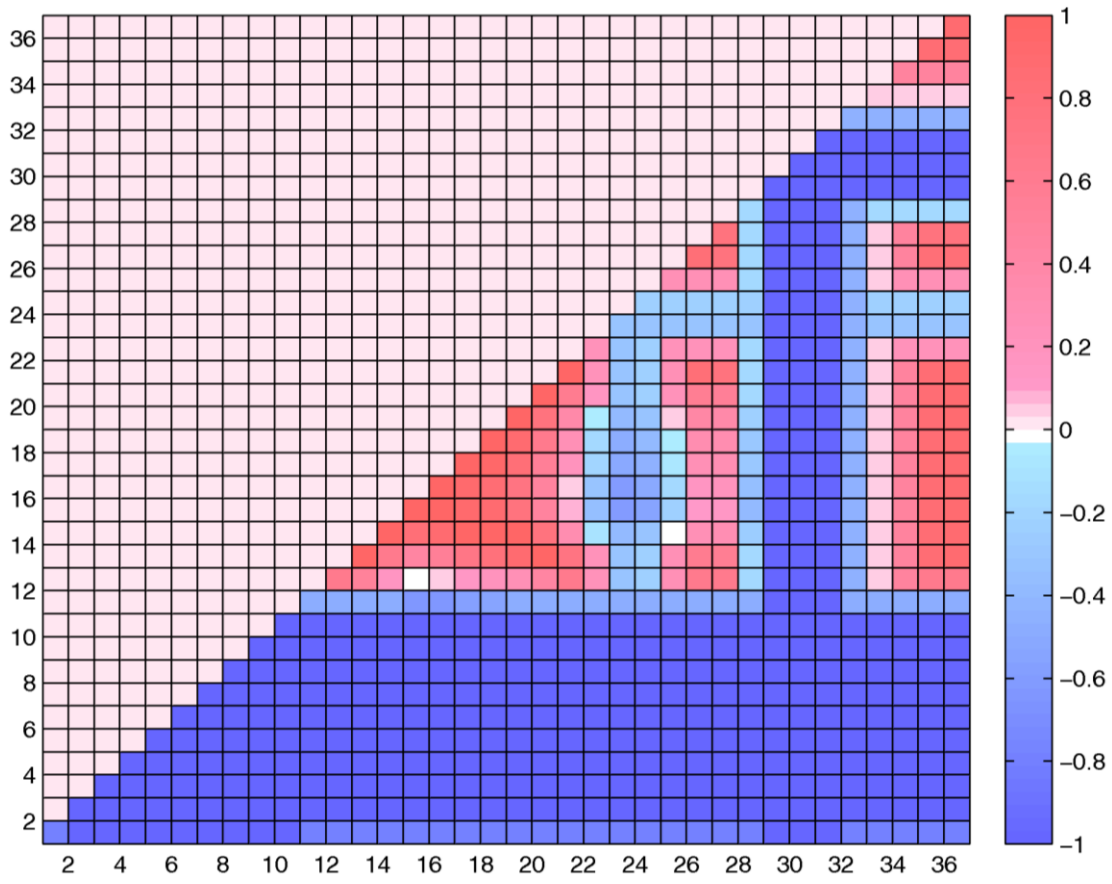

Figure 28: Pairwise consistency plots for the first level of assumptions on the uncertainty.

Height: 30 mm.

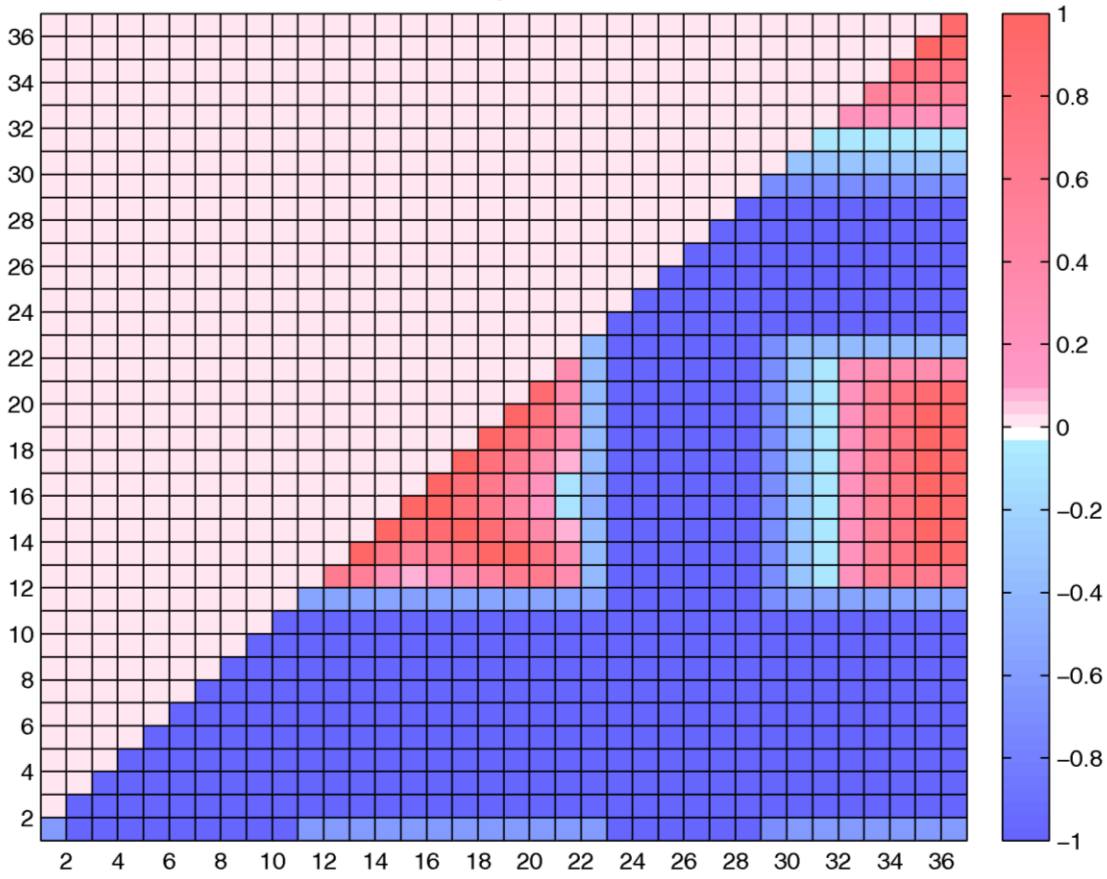

Figure 29: Pairwise consistency plots for the first level of assumptions on the uncertainty.

Height: 45 mm.

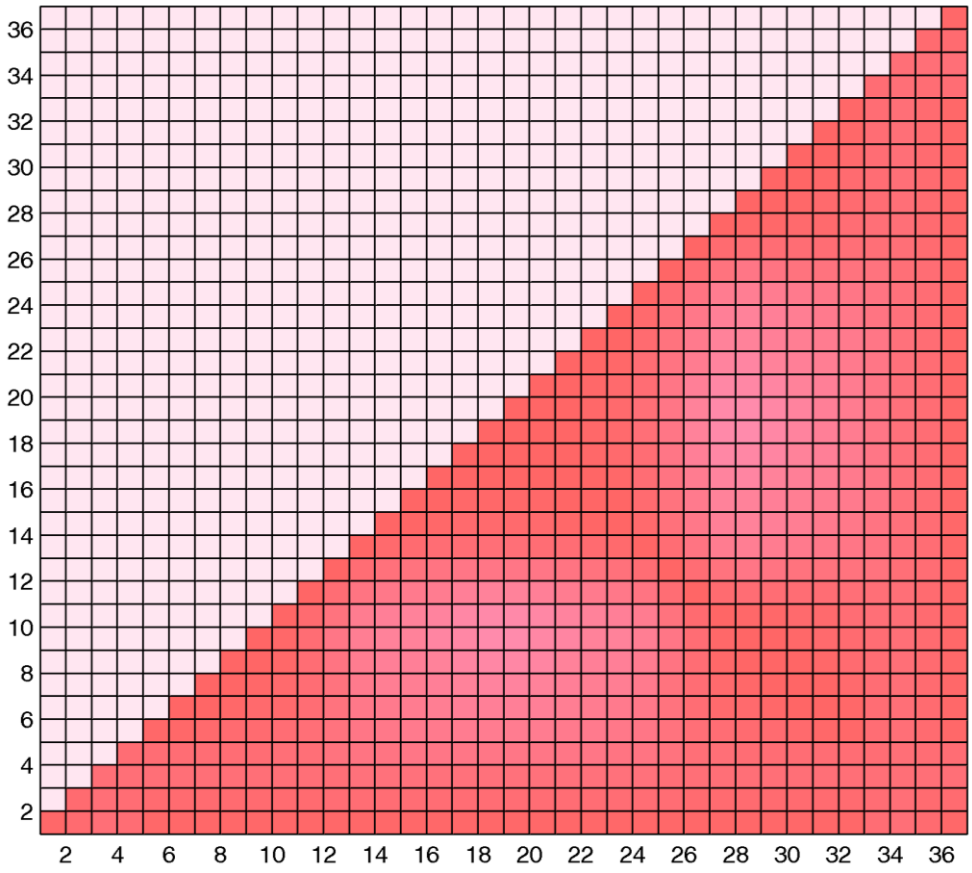

Figure 30: Pairwise consistency plots for the second level of assumptions on the uncertainty. Height: 15 mm.

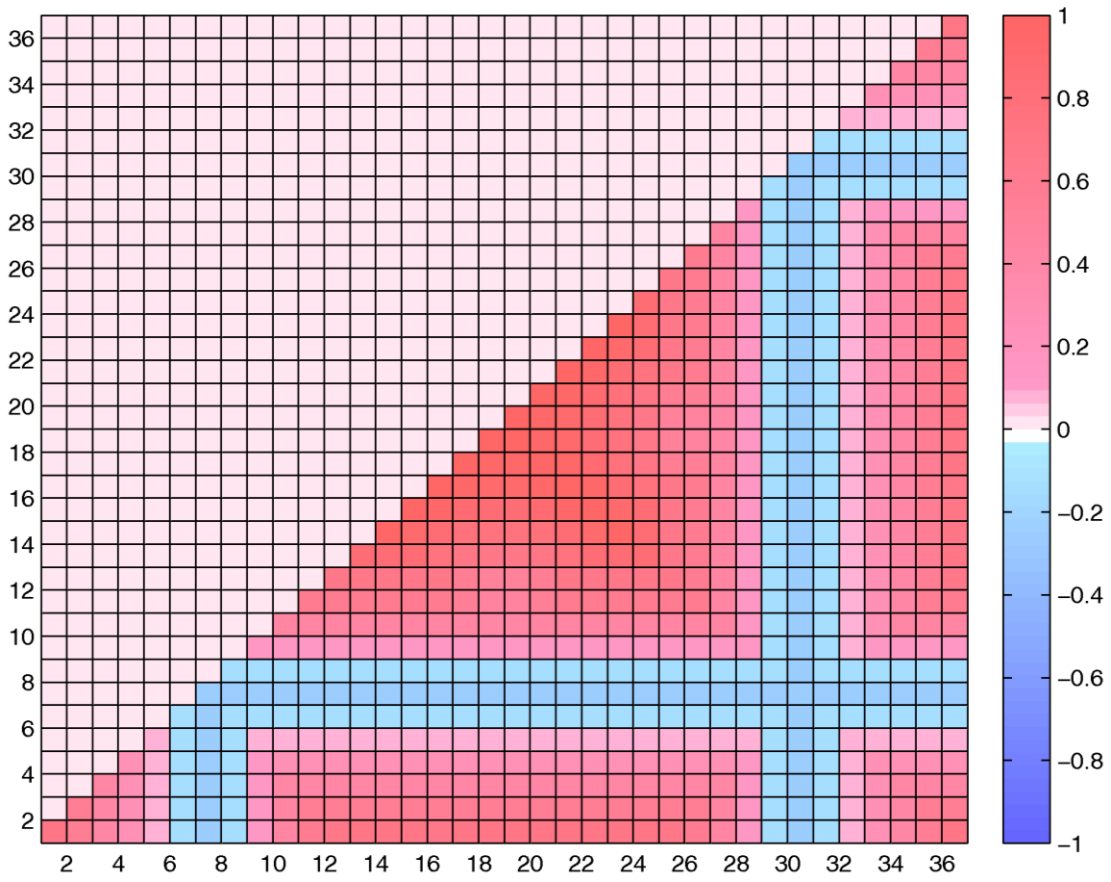

Figure 31: Pairwise consistency plots for the second level of assumptions on the uncertainty. Height: 30 mm.

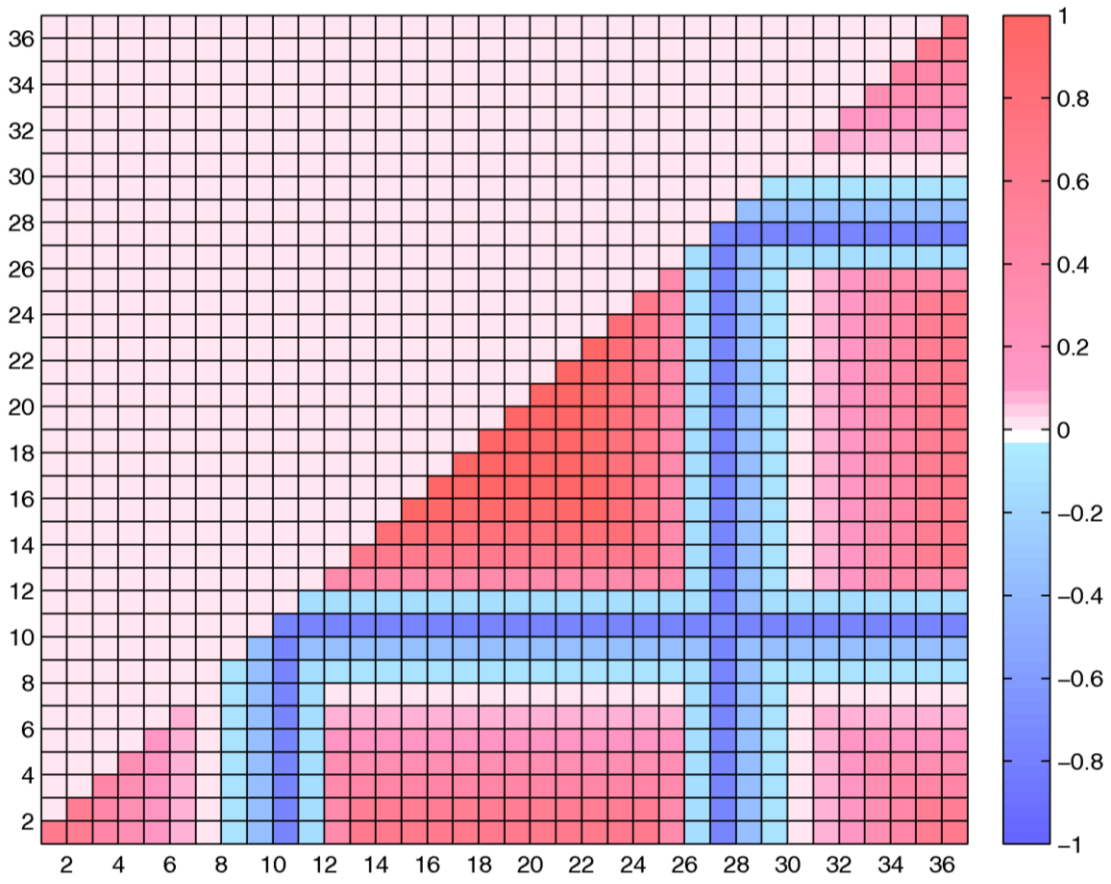

Figure 32: Pairwise consistency plots for the second level of assumptions on the uncertainty. Height: 45 mm.

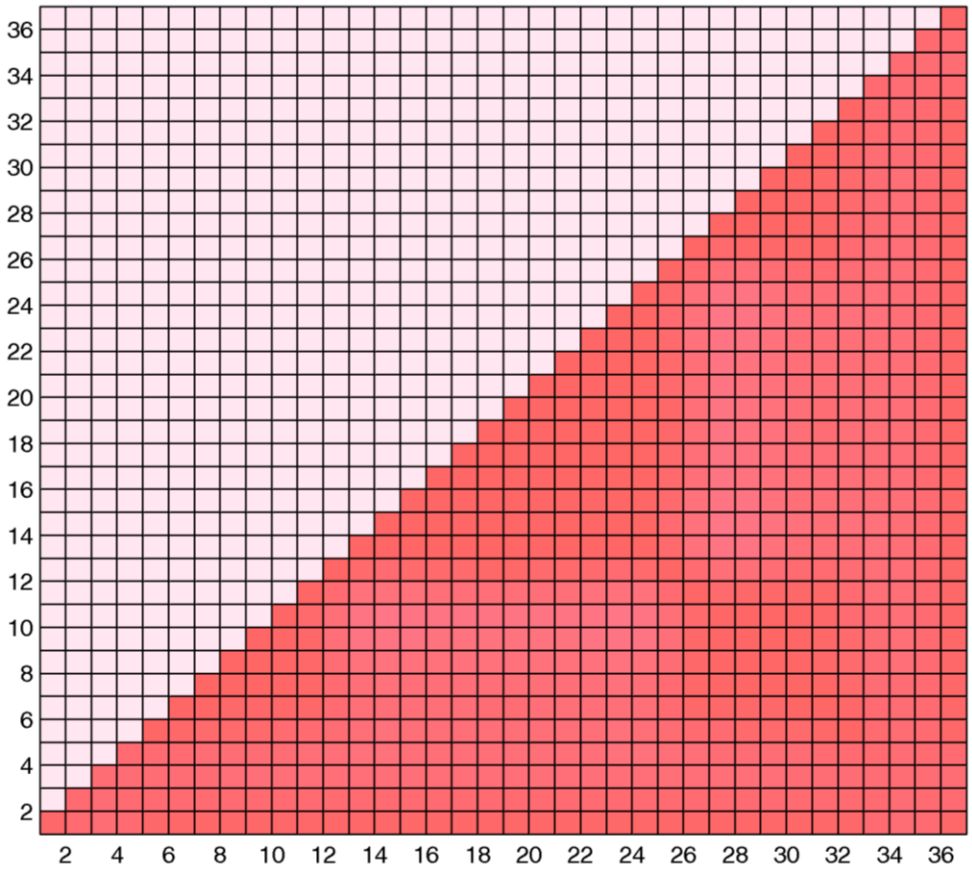

Figure 33: Pairwise consistency plots for the third level of assumptions on the uncertainty. Height: 15 mm.

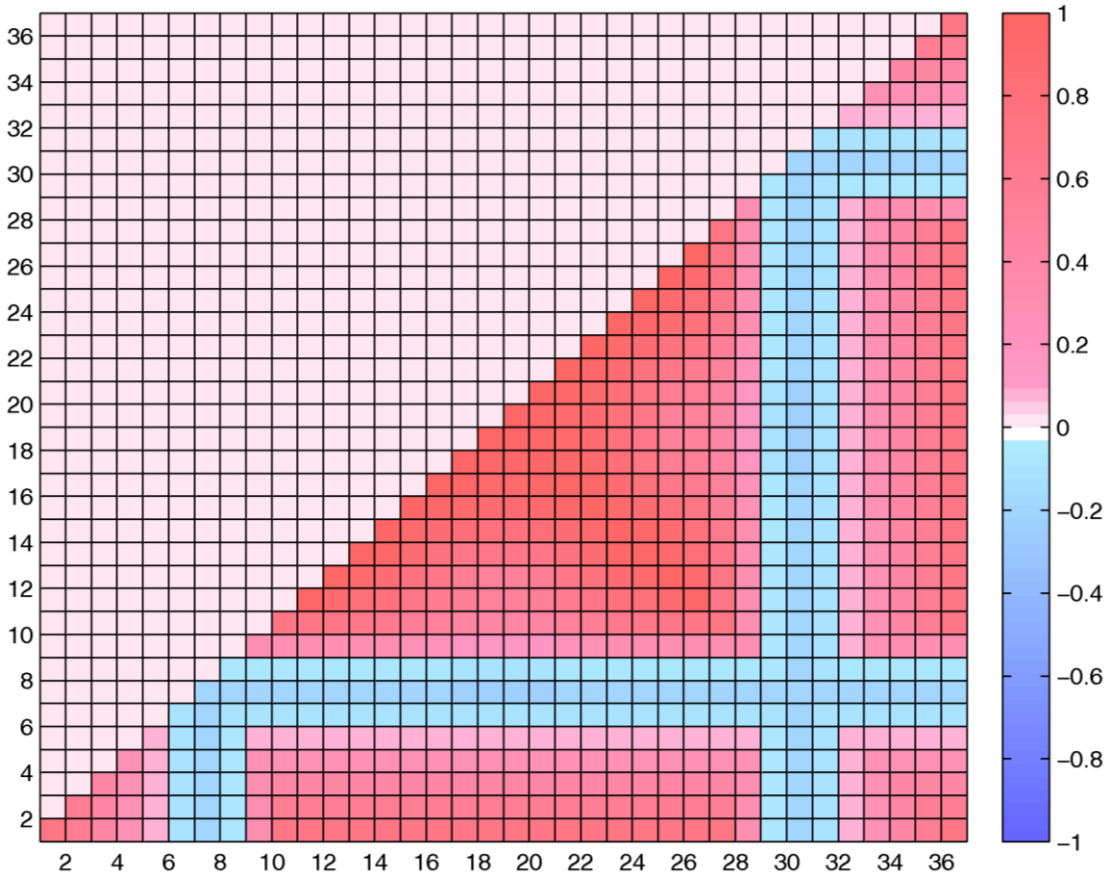

Figure 34: Pairwise consistency plots for the third level of assumptions on the uncertainty. Height: 30 mm.

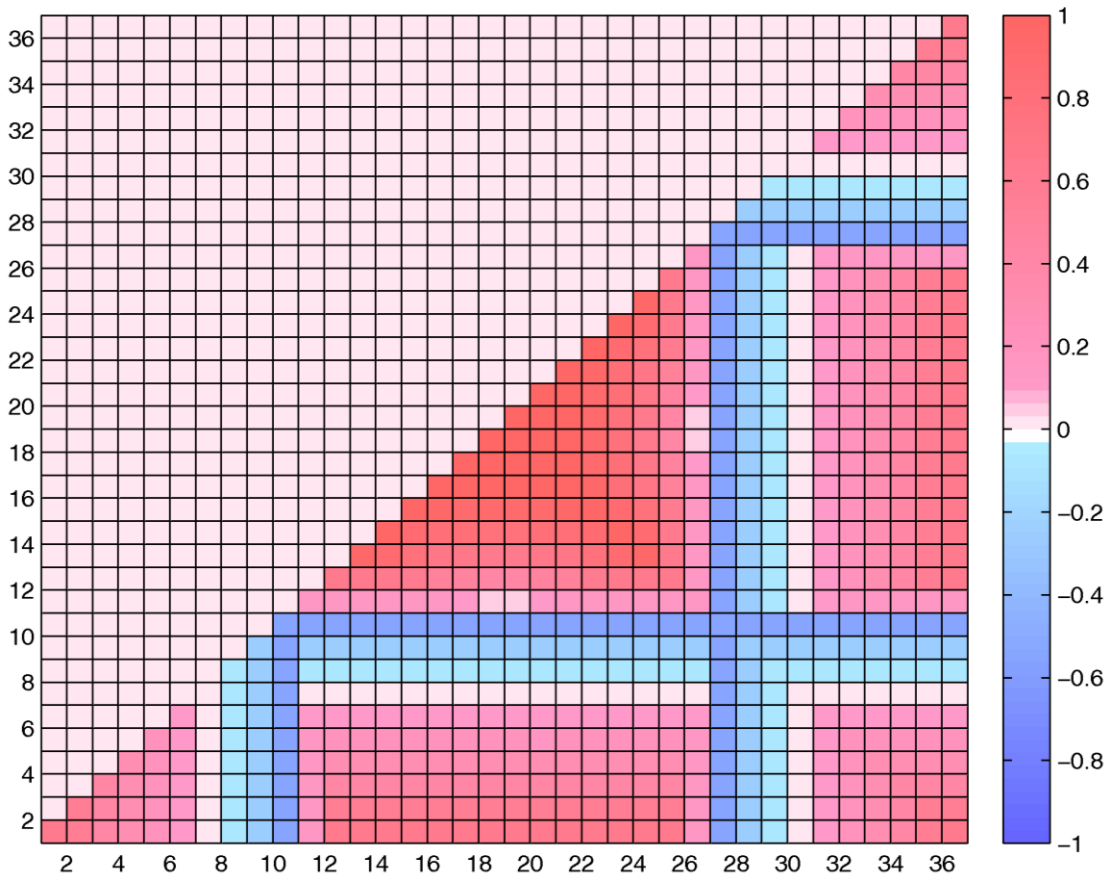

Figure 35: Pairwise consistency plots for the third level of assumptions on the uncertainty. Height: 45 mm.

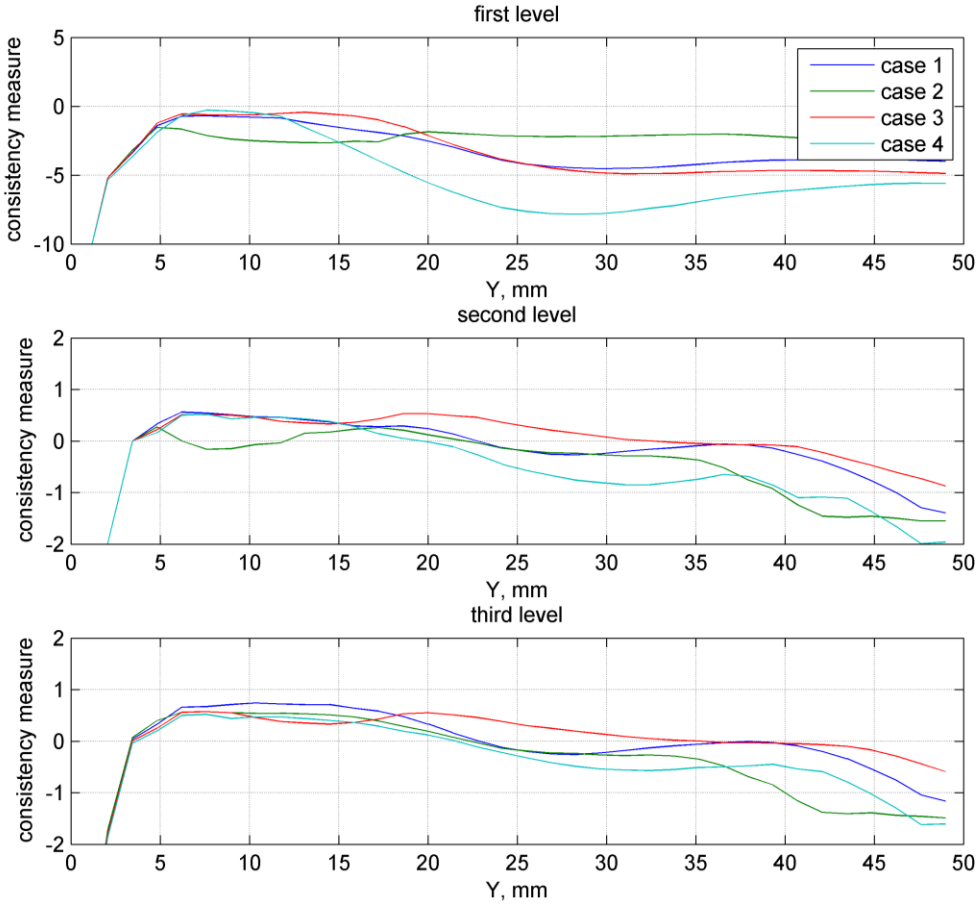

Figure 36: The overall consistency measure defined as the smallest pairwise consistency measure in a pairwise test versus height.

Table 2: Comparison of the spectral analysis-derived properties determined from the phase maps unwrapped by PUMD relative to the values from the phase maps unwrapped by PUWM.

	puffing frequency, Hz			time lag, ms			SNR		
	Y = 15 mm	Y = 30 mm	Y = 45 mm	Y = 15 mm	Y = 30 mm	Y = 45 mm	Y = 15 mm	Y = 30 mm	Y = 45 mm
case 1									
X = -16.1 mm	0	0	0	0	3.56	-1.15	-19.17	112.92	95.93
center	0	0	0	0	2.32	-1.11	-532.87	-434.13	-184.03
X = 16.1 mm	0	0	0	0	0	0.81	-101.58	-5.23	21.52
case 2									
X = -16.1 mm	-0.28	0.01	0.01	0	29.42	5.43	30.34	14.94	16.58
center	0.01	0.01	0.01	0	0	0	-11.83	-7.84	-7.54
X = 16.1 mm	0.01	0.01	0.01	0	0	0	7.07	-1.76	11.04
case 3									
X = -16.1 mm	0.13	0.13	0.13	0	-1.26	-0.63	-613.91	-678.89	-720.39
center	0.13	0.13	0.13	0	0.49	0.45	-684.75	-841.23	-649.74
X = 16.1 mm	0.13	0.13	0.13	0	0	0	50.36	8.02	6.4
case 4									
X = -16.1 mm	0	0	0	0	-0.96	-2.36	-56.9	-82.6	309.5
center	0	0	0	0	2.82	1.1	205.9	447.3	251.7
X = 16.1 mm	0	0	0	0	0	0	101.09	117.97	-38.529

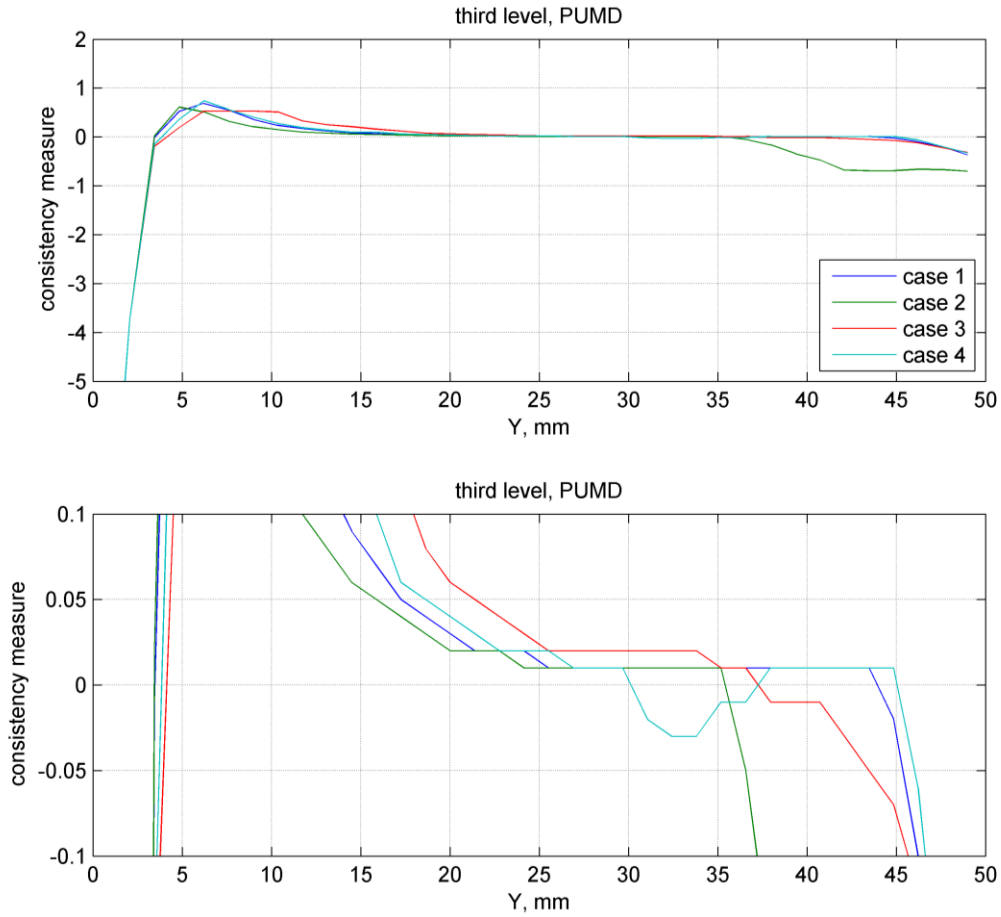

Figure 37: Overall pairwise consistency measure profiles of phase data unwrapped by PUMD. The bottom plot shows a zoomed-in detail.

CHAPTER 4

CONCLUSIONS AND FUTURE WORK

The usefulness of advanced image processing and fringe pattern analysis of fringe images produced by holographic interferometry for the validation and uncertainty quantification of the CFD model Arches has been investigated. It has been found that the phase demodulation and phase unwrapping techniques can produce valuable high-resolution (both spatially and temporally) data for V/UQ purposes. The error and uncertainty approximation of a detailed and refined image processing and fringe pattern analysis method has been carried out. The unwrapped phase data along with determined lower and upper uncertain bounds has been used for consistency analysis. Pairwise consistency tests have been run and the results are presented in this thesis. A number of levels of assumptions on experimental and simulation uncertainties have been tried, along with two different phase unwrapping algorithms. No combination of these resulted in fully pairwise consistent data. It has been concluded that additional simulations are needed to take into account the possible ambient impurities observed in experiments.

As mentioned before, additional simulation cases have been designed and initiated at the time of the submittal of this thesis. These cases have been designed to introduce the effect of helium diffusing into the ambience to mimic the effect observed in experimental results.

The preliminary consistency analysis presented in this work provided other useful conclusions on the consistency analysis methodology itself. It has to be noted that while the PUMD unwrapper has proven to be less reliable than the PUWM unwrapper, it produced more consistent results due to its higher inherent uncertainties. This leads to the conclusion that the consistency measure proposed by Feeley et al. (47) is not the most meaningful in this application, since it does not take into account the amount of inherent uncertainty in the nominal values. Therefore developing and proposing a new consistency measure definition might be necessary.

REFERENCES

1. Fay, J. A. Buoyant Plumes and Wakes. *Annual Review of Fluid Mechanics* **1973**, 5, 151-160

2. Rodi, W. Turbulent Buoyant Jets and Plumes. *International Journal of Heat and Fluid Flow* **1982**, 3, 194

3. List, E. J. Turbulent Jets and Plumes. *Annual Review of Fluid Mechanics* **1982**, 14, 189-212

4. Papanicolau, P. A.; List, E. J. Investigations of Round Vertical Turbulent Buoyant Jets. *Journal of Fluid Mechanics* **1988**, 195, 342-391

5. Dai, Z; Tseng, L. K.; Faeth, G. M. Structure of Round, Fully Developed Buoyant Turbulent Plumes. *Journal of Heat Transfer* **1994**, 116, 116

6. Hamins, A.; Yang, J. C.; Kashiwagi, T. An Experimental Investigation of the Pulsating Frequency of Flames. *Proceedings of the Combustion Institute* **1992**, 24, 1695-1705

7. Subbarao, E. R.; Cantwell, B. J. Investigation of a Co-flowing Buoyant Jet: Experiments on the Effects of Reynolds Number and Richardson Number. *Journal of Fluid Mechanics* **1992**, 245, 69-90

8. Cetegen, B. M.; Ahmed, T. A. Experiments on the Periodic Instability of Buoyant Plumes and Pool Fires. *Combustion and Flame* **1993**, 93, 157-184

9. Cetegen, B. M.; Kasper, K. D. Experiments on the Oscillatory Behavious of Buoyant Plumes of Helium and Helium-air Mixtures. *Physics and Fluids* **1996**, 8, 2974-2984

10. Boulanger, J. Laminar Round Jet Diffusion Flame Buoyant Instabilties: Study on the Disappearance of Varicose Structures at Ultra-low Froude Number. *Combustion and Flame* **2010**, 157, 757-768

11. Hariharan, P. *Basics of Interferometry*, 1st ed.; Academic Press, 1991

12. Magnussen, S. PhD. Dissertation, University of Bergen, 2004

13. Villa, J.; De la Rosa, I.; Miramontes, G.; Quiroga, J. A. Phase Recovery from a Single Fringe Pattern Using an Orientational Vector-field-regularized Estimator. *Journal of the Optical Society of America* **2005**, 22, 2766-2773

14. Falih, A. H.; Castellane, R. M. Interferogram Phase Evaluation through a Differential Equation Technique. *Computers and Electrical Engineering* **2004**, 30, 605-614

15. Tay, C. J.; Quan, C.; Yang, F. J.; He, X. Y. A New Method for Phase Extraction from a Single Fringe Pattern. *Optics Communications* **2004**, 239, 251-258

16. Wang, Boxiong; Shi, Yuqing; Pfeifer, T.; Mischo, H. Phase Unwrapping by Blocks. *Measurement* **1999**, 25, 285-290

17. Pritt, M. D. Phase Unwrapping by Means of Multigrid Techniques for Interferometric SAR. *IEEE Transactions on Geoscience and Remote Sensing* **1996**, 34, 728-738

18. Barrett, H. H.; Myers, K. J. *Foundations of Image Science*, 1st ed. Wiley, 2003

19. Buades, A.; Coll, B.; Morel, J. M. A Review of Image Denoising Algorithms, with a New One. *Multiscale Modeling and Simulation* **2005**, 4, 490-530

20. Anjali, P.; Ajay, S.; Sapre, S. D. A Review on Natural Image Denoising Using Independent Component Analysis (ICA) Technique. *Advances in Computational Research* **2010**, 2, 6-14

21. Ruderman, D. L. The Statistics of Natural Images. *Computation in Neural Systems* **1994**, 5, 517-548

22. Cheng, H. D; Shi, X. J. A Simple and Effective Histogram Equalization Approach to Image Enhancement. *Digital Signal Processing* **2004**, 14, 158-170

23. Foracchia, M.; Grisan, E.; Ruggeri, A. Luminosity and Contrast Normalization in Retinal Images. *Medical Image Analysis* **2005**, 9, 179-190

24. Quiroga, J. A.; Servin, M. Isotropic N-dimensional Fringe Pattern Normalization. *Optics Communications* **2003**, 224, 221-227

25. Kreis, T. Digital Holographics Interference-phase Measurement Using the Fourier-transform Method. *Journal of the Optical Society of America* **1986**, 3, 847-855

26. Quan, C.; Hiu, N.; Tay, C. J. An Improved Windowed Fourier Transform for Fringe Demodulation. *Optics and Laser Technology* **2010**, 42, 126-131

27. Quan, C.; Chen, W.; Tay, C. J. Phase-retrieval Techniques in Fringe Projection Profilometry. *Optics and Lasers in Engineering* **2010**, 48, 235-243

28. Servin, M.; Quiroga, J. A.; Marroquin, J. L. General N-dimensional Quadrature Transform and its Application to Interferogram Demodulation. Journal *of the Optical Society of America* **2003**, 20, 925-934

29. Itoh, K. Analysis of the Phase Unwrapping Algorithm. *Applied Optics* **1982**, 21, 2470

30. Goldstein, R. M.; Zebker, H. A.; Werner, C. L. Satellite Radar Interferometry: Two-dimensional Phase Unwrapping. *Radio Science* **1988**, 23, 713-720

31. Flynn, T. J. Two-dimensional Phase Unwrapping with Minimum Weighted Discontinuity. *Journal of the Optical Society of America* **1997**, 14, 2692-2701

32. Estrada, J. C.; Servin, M.; Vargas, J. 2D Simultaneous Phase Unwrapping and Filtering: A Review and Comparison. *Optics and Lasers in Engineering*, article in press

33. Ghiglia, D. C.; Mastin, G. A.; Romero, L. A. Cellular-automata Method for Phase Unwrapping. *Journal of the Optical Society of America* **1986**, 4, 267-280

34. Ghiglia, D. C.; Romero, L. A. Robust Two-dimensional Weighted and Unweighted Phase Unwrapping that Uses Fast Transforms and Iterative Methods. *Journal of the Optical Society of America* **1994**, 11, 107-117

35. Marroquin, J. L.; Rivera, M. Quadratic Regularization Funcionals for Phase Unwrapping. *Journal of the Optical Society of America* **1995**, 12, 2393-2400

36. Marroquin, J. L. Parallel Algorithms for Phase Unwrapping Based on Markov Random Field Models. *Journal of the Optical Society of America* **1995**, 12, 2578-2585

37. Oberkampf, W. L.; Roy, C. J. *Verification and Validation in Scientific Computing*, 1st ed. Cambridge, 2010

38. Bayarri, M. J.; Berger, J. O.; Paulo, R.; Sacks, J.; Cafeo, J. A.; Cavendish, J.; Lin, C. H.; Tu, J. *A Framework for Validation of Computer Models*; Institute of Statistical Sciences, **2005**

39. Roy, C. J.; Oberkampf, W. L. A Comprehensive Framework for Verification, Validation and Uncertainty Quantification in Scientific Computing. *Computational Methods in Applied Mechanical Engineering* **2011**, 200, 2131-2144

40. Schönbucher, A.; Arnold, B.; Banhardt, V.; Bieller, V.; Kasper, H.; Kaufmann, M.; Lucas, R.; Schiess, N. Simultaneous Observation of Organized Density Structures and the Visible Field in Pool Fires. *Symposium (International) on Combustion* **1988**, 21, 83-92

41. Eldredge, W. PhD. Dissertation, University of Utah, 2011

42. Incropera, P. F.; Dewitt, D. P. *Fundamentals of Heat and Mass Transfer*, 1st ed. Wiley, 2002

43. Reichenberg, D. *New Simplified Methods for the Esimation of the Viscosities of Gas Mixtures at Moderate Pressures*; National Engineering Laboratory, 1977

44. Wilke, C.; Lee, C. Estimation of Diffusion Coefficients for Gases and Vapors. *Industrial and Engineering Chemistry* **1955**, 47, 1253

45. Qifeng, Y.; Liu, X.; Sun, X. Generalized Spin Filtering and an Improved Derivative-sign Binary Image Method for the Extraction of Fringe Skeletons. *Applied Optics* **1998**, 37, 4505-4509

46. Guerrero, J. A.; Marroquin, J. L.; Rivera, M.; Quiroga, J. A. Adaptive Monogenic Filtering and Normalization of ESPI Fringe Patterns. *Optics Letters* **2005**, 30, 3018-3020

47. Feeley, R.; Seiler, P.; Packard, A.; Frenklach, M. Consistency of a Reaction Dataset. *Journal of Physical Chemistry A* **2004**, 108, 9573-9583